Deep-Sea Research I 100 (2015) 140–158

Contents lists available at ScienceDirect

Deep-Sea Research I

journal homepage: www.elsevier.com/locate/dsri

Instruments and Methods

Characterization of the uncertainty of loop current metrics using a multidecadal numerical simulation and altimeter observations

Dmitry S. Dukhovskoy [a,*], Robert R. Leben [b], Eric P. Chassignet [a], Cody A. Hall [b], Steven L. Morey [a], Robert Nedbor-Gross [a]

[a] Center for Ocean-Atmospheric Prediction Studies (COAPS), Florida State University, 2000 Levy Avenue, Building A, Suite 292, Tallahassee, FL 32310, USA
[b] Colorado Center for Astrodynamics Research, University of Colorado, ECNT 320, 431 UCB, Boulder, CO 80309-0431, USA

ARTICLE INFO

Article history:
Received 13 August 2014
Received in revised form
8 January 2015
Accepted 14 January 2015
Available online 23 February 2015

Keywords:
Eddies and mesoscale processes
Gulf of Mexico
Loop Current
Satellite altimetry
Ocean modeling
Ocean front detection

ABSTRACT

Satellite altimetry is routinely used to monitor Loop Current intrusion and eddy shedding in the Gulf of Mexico. Statistical estimates of the location and variability of the Loop Current vary significantly among published studies and it is not obvious whether these differences are caused by observational errors, different analysis methodologies, processing and gridding of altimeter data products, or the highly variable nature of the Loop Current system itself. This study analyzes the uncertainty of basic Loop Current statistical estimates derived from altimeter observations, i.e. the northern and western extent, the mean Loop Current eddy separation period, and the relationship between the Loop Current retreat latitude and eddy separation period. The robustness of these statistics is assessed using sea surface height data from a 1/25° free-running multidecadal numerical simulation of the Gulf of Mexico HYbrid Coordinate Ocean Model. A suite of sensitivity tests is performed to identify sources of uncertainty in the Loop Current statistics. The tests demonstrate that the Loop Current metrics from the altimeter fields are less sensitive to the choice of the reference sea surface height mean field or Loop Current front definition than to satellite sampling patterns. Analysis of the model and altimetry-derived sea surface height fields shows that the Loop Current variability changes between regimes of rapid and slow eddy formation cycles. This analysis leads to a discussion of the stationarity of the LC system. The mean separation period estimated from the altimeter fields for 1993–2010 is 8 ± 1.8 months. This uncertainty is larger than the errors introduced by the satellite data processing and gridding technique, which is on the order of O (1 month). It is shown that the available altimetry observational record is not long enough at this time to be able to estimate the mean separation period within one-month uncertainty.

1. Introduction

The Gulf of Mexico (GoM) is a semi-enclosed sea characterized by strong mesoscale eddying currents associated with the Loop Current (LC), which is the dominant ocean circulation feature in the region. The LC forms as warm Caribbean water enters the GoM through the Yucatan Channel, loops anticyclonically within the deep basin, and exits through the Straits of Florida. The LC exhibits a wide range of variability in its configuration and position. During a retracted phase, the LC only slightly intrudes into the GoM, turns promptly east, and exits the Gulf through the Straits of Florida. When extended further north and west, the LC sheds large warm-core anticyclonic vortices commonly called Loop Current Eddies (LCEs). The time interval between eddy separation events (which is commonly referred to as the eddy separation period even though this is not a strictly periodic process) has been observed to range from as short as a few weeks to as long as 18–19 months (Leben, 2005; Vukovich, 2012).

Since 1992, altimetry observations have become routinely available for analysis (Wunsch and Stammer, 1998). Of the three primary satellite products currently used for observing the ocean mesoscale – altimetry, ocean color, and sea surface temperature – satellite altimetry provides the most complete observational record for quantitative monitoring of GoM mesoscale circulation and LC variability (see "Remote Sensing Overview" in Donohue et al. (2008)). The LC and LCE statistics derived from altimetry are widely used for monitoring the complex mesoscale dynamics in the GoM and for evaluating the skill of hydrodynamic models of general circulation in the Gulf. The LC state can be described in terms of well-defined metrics that are used to quantify the statistical characteristics of the LC and LCEs. These metrics are obtained from altimetric observations

* Correspondence to: Center for Ocean-Atmospheric Prediction Studies (COAPS), Florida State University, 2000 Levy Avenue, Suite 257, Research Building A, Tallahassee, FL 32306-2741, USA. Tel.: +1 850 644 1168.
E-mail addresses: ddukhovkosy@fsu.edu (D.S. Dukhovskoy), leben@Colorado.edu (R.R. Leben), echassignet@fsu.edu (E.P. Chassignet), codyalanhall@gmail.com (C.A. Hall), smorey@fsu.edu (S.L. Morey), rnedbor1@ufl.edu (R. Nedbor-Gross).

http://dx.doi.org/10.1016/j.dsr.2015.01.005
0967-0637/

of sea surface height anomaly (SSHA) added to a mean sea surface height (SSH) field representative of the mean ocean circulation (Leben, 2005). Representative statistics include the spatial probability distribution of the LC in the GoM, the northern- and westernmost positions of the LC, and LCE separation, propagation and dissipation (Sturges, 1994; Vukovich, 1995; Sturges and Leben, 2000; Leben, 2005; Vukovich, 2007, 2012).

Discrepancies in LC and LCE statistics exist, however, among published studies (e.g., Leben, 2005; Vukovich, 2007, 2012; Hamilton et al., 2015). This disagreement may arise from a number of factors. Differences in methodologies employed for constructing gridded SSH fields, LC tracking, defining the LC frontal position, and handling missing observations may lead to a different result using the same set of observations. Published studies are also based on different sets of observational records.

The major goal of this study is to analyze the uncertainty of basic LC statistics derived from SSH observations, i.e. the northern and western extent, the mean LCE separation period, and the relationship between the LC retreat latitude and eddy separation period. A regional, free-running multi-decadal (54 years) HYbrid Coordinate Ocean Model (HYCOM) (Bleck, 2002; Chassignet et al., 2003) run configured for the GoM (Section 2.1) is used to characterize uncertainties of the LC statistics derived from SSH fields (Section 3.2). In this analysis, the modeled SSH is used to assess sensitivity of the LC statistical estimates to various factors. This approach eliminates uncertainty related to observational errors because the "true" state of the field being sampled is known and is given by SSH simulated by the numerical model. It is worth mentioning that the intent of the study is not to compare observed LC statistics to the model (or vice versa) but to use the multidecadadal simulation to estimate uncertainties of the LC statistics derived from altimetry-based SSH fields.

The following sources of uncertainties in the LC statistics are considered in this paper: definition of the LC front (Section 3.3), choice of the reference SSH mean field (Section 3.4), and altimeter sampling and data processing (Section 3.5). This study does not consider random and systematic errors related to instrument, orbital, atmospheric, sea state, tidal, and marine geoid corrections to the satellite altimeter range measurement (Shum et al., 1995; Chelton et al., 2001).

The study demonstrates that the LC statistics are highly sensitive to the satellite sampling patterns suggesting that satellite sampling is the largest source of uncertainty in the altimeter-derived SSH fields. Weaker sensitivity of the LC statistical estimates is found in the tests with a different reference SSH mean field and alternative LC front definition. This study provides a new insight into the behavior of the LC system in the GoM at longer time scales than previously studied. The choice of the analyzed time period and the record length of the observations impact the LC mean separation period estimates and the relationship between separation period and the retreat latitude of the LC. This leads to a discussion of the stationarity of the LC system in the CCAR altimetry-derived SSH data record (Section 4) and in the model (Section 5).

2. Methods

2.1. The numerical simulation

The 1/25° regional HYCOM Gulf of Mexico domain (hereafter referred as GoM-HYCOM) is configured from 18.9°N to 31.96°N and from 98°W to 76.4°W (Fig. 1a). The vertical grid uses 20 hybrid layers, which are mainly isopycnal layers in the open ocean below the mixed layer (see complete description of the hybrid coordinate system in Chassignet et al. (2003, 2006)). The target densities, which define the vertical grid in the model, represent the density range of water masses in the GoM and western Caribbean (Fig. 1b). The vertical grid is configured such that the upper ocean gains most of the vertical resolution (Fig. 1d and e) and is able to represent the major features of the vertical structure of the flow through the Yucatan Channel and the Straits of Florida (Fig. 1e and f). Assuming that the vertical extent of the LC is limited by the deepest isopycnal layer in the Straits of Florida (shallower than 900 m between Florida and Bahamas), the LC is resolved by 17 of the 20 hybrid layers in the model (Fig. 1f). Model bathymetry is derived from the Naval Research Laboratory Digital Bathymetry Data Base 2-min resolution (NRL DBDB2; www.7320.nrlssc.navy.mil/DBDB2_WWW). Monthly climatology river inflow is simulated at 40 locations along the coast. More details of the model parameters are listed in Table 1 (see also the model description at hycom.org/dataserver/goml0pt04).

A model nesting approach similar to that of Zamudio and Hogan (2008) is adopted in this study. GoM-HYCOM has open boundary conditions derived from a bi-weekly climatology produced by four years (2000–2003) of a free-running simulation of the 1/12° Atlantic HYCOM. The 1/12° Atlantic HYCOM, used as the outer model, covers the domain from 27.9°S to 70°N and from 98°W to 36.2°E. Fig. 1c shows volume fluxes across the open boundaries of the inner model GoM-HYCOM that are derived from the 1/12° Atlantic HYCOM. It is noteworthy that no interannual variability is imposed at the lateral open boundaries.

The simulation is initialized from a 5-year spin-up run that started from rest with the Generalized Digital Environmental Model 3.0 (GDEM) climatological fields forced with atmospheric fields from the Fleet Numerical Meteorology and Oceanography Center's Navy Operational Global Atmospheric Prediction System (NOGAPS) (Rosmond et al., 2002). Following spin-up, atmospheric forcing (10-m wind speed, vector wind stress, 2-m air temperature, 2-m atmospheric humidity, surface shortwave and longwave heat fluxes, and precipitation) is derived from hourly fields of the Climate Forecast System Reanalysis (CFSR) (Saha et al., 2010) from 1992 through 2009. Surface latent and sensible heat fluxes, along with evaporation, are calculated using bulk formulas during model run time. The bulk transfer coefficients are parameterized following Kara et al. (2000) algorithm. This 18-year record of surface forcing is repeated three times (three cycles) to produce the continuous 54-year model integration. The ends of the 18-year surface forcing time series are blended by temporal interpolation of the last three days in 2009 towards the forcing fields on January 1, 1992 in order to prevent shocks in forcing between cycles in the 54-year record. The surface forcing is used in this way to realistically mimic the stochastic nature of atmospheric forcing.

The modeled Yucatan transport is about 29 Sv (Fig. 2a), which is within the range of published transport estimates that range from 23.8 ± 1 Sv (Sheinbaum et al., 2002) to 30.3 ± 5 Sv (Rousset and Beal, 2010). The model exhibits only moderate interannual variability in the Yucatan transport, which is not surprising given the lack of interannual variability at the open boundaries.

The mean Yucatan Channel flow from the model (Fig. 2b) has a structure similar to that reported by observational studies (Abascal et al., 2003; Sheinbaum et al., 2002). The strong Yucatan Current, the prominent feature in the channel, flows northward predominantly above 1000 m, and its core has speeds exceeding 1 m/s. The mean flow below $\sim$1200 m, often represented by a single model layer, is slower than observed with near-zero velocities (< 0.05 m/s) in both directions. The standard deviation of the deep flow (> 0.025 in the central and eastern parts of the channel) demonstrates the existence of negative and positive fluctuations of the deep flow. The core speed and location show substantial temporal variability (Fig. 2c). The vertical spatial structure of the Yucatan flow variability in the model is well explained by the first two Empirical Orthogonal Function (EOF) modes (Fig. 2d and e). Both modes describe intensification and

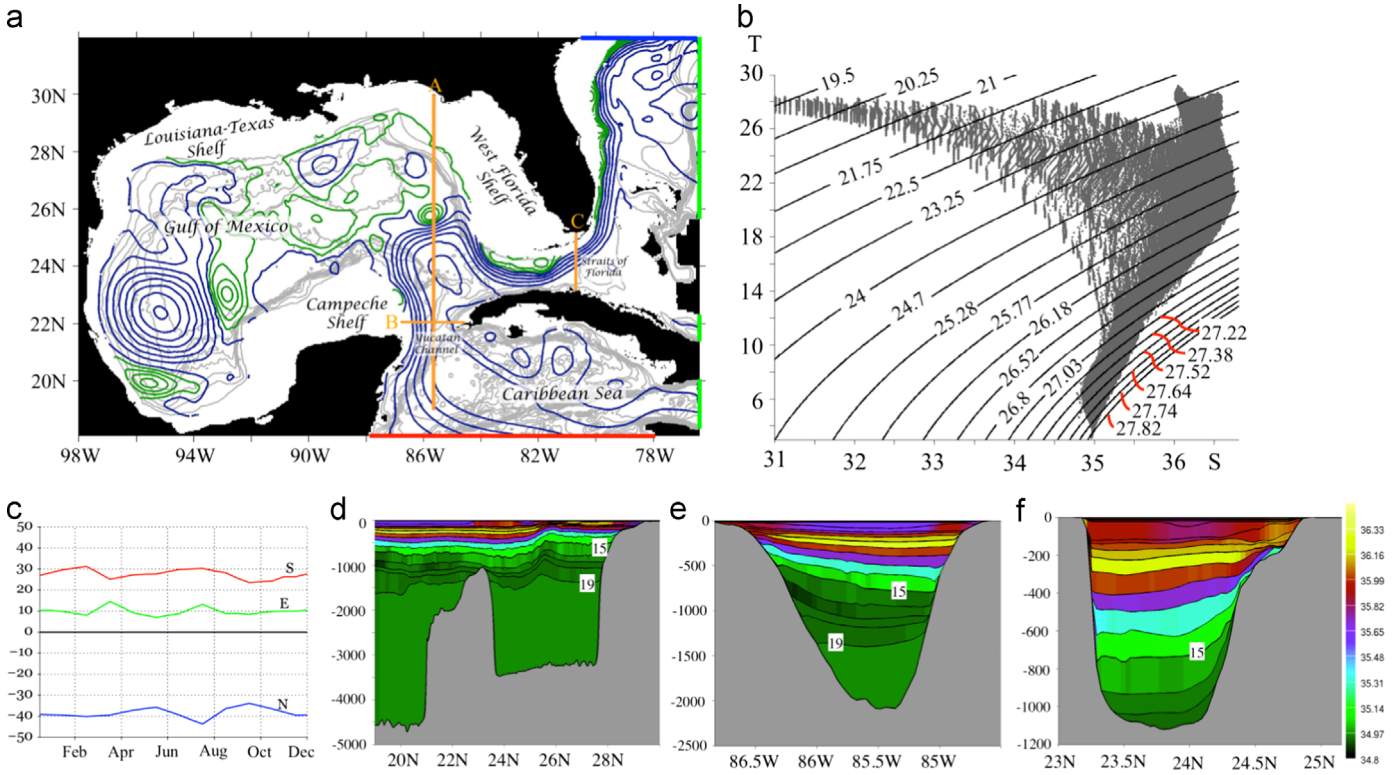

Fig. 1. (a) The Gulf of Mexico HYCOM model domain (GoM-HYCOM). The contour lines are instantaneous positive (blue) and negative (green) SSH contours from a single model output time. Input from the 1/12° Atlantic HYCOM is imposed at the open boundaries shown with red, green, and blue lines. The orange lines are cross-sections shown in (d–f). (b) *T–S* diagram of GDEM3 July climatology for the northwest Caribbean Sea and the Gulf of Mexico for depths from 30 m to 4000 m. The contours are HYCOM target densities (σ_0) used to configure the vertical grid in the simulation. (c) Volume fluxes (Sv) along the GoM-HYCOM open boundaries calculated from the nesting climatology velocity fields derived from the 1/12° Atlantic HYCOM during one year. Positive flux is into the model domain. Vertically integrated fluxes are presented for three open boundaries: (red) Southern, (green) Eastern, and (blue) Northern. The abscissa is time (months). (d–f) Vertical distribution of the model salinity and interfaces of the hybrid vertical layers in the cross-sections along lines A–C shown in (a). Bottom interfaces of the layers 15 and 19 are marked. The ordinate is depth (m), the abscissa is latitude or longitude, and different vertical and spatial scales are used in each plot. The deepest isopycnal layer, 18, in (f) does not connect to the North Atlantic due to the shallower depths in the Straits of Florida outside the Gulf of Mexico. (For interpretation of the references to color in this figure legend, the reader is referred to the web version of this article.)

Table 1
GoM-HYCOM characteristics.

Characteristics	GoM-HYCOM
HYCOM version	2.2.18
Horizontal spacing	Mercator grid: 0.04° in longitude × 0.04° cos(latitude) in latitude
Bathymetry	DBDB2
Number of grid nodes	385 × 541
Vertical coordinates	20 hybrid layers
Reference density (σ_0)	25.0
Baroclinic time step	240.0 s
Barotropic time step	7.5 s
Quadratic bottom friction	2.2e − 3
Thickness of bottom boundary layer	10 m
Surface salinity relaxation	Generalized Digital Environmental Model–V3.0 (GDEM3)
Scalar horizontal advection	Second-order flux-corrected transport
Momentum advection	Second-order flux-corrected transport
Boundary condition	Non-slip
Vertical turbulence	KPP

weakening of the flow in the upper channel resulting from west–east migration of the current, in general agreement with Ezer et al. (2003). The three-banded pattern of the 1st EOF mode also agrees with Bunge et al. (2002). In some years, the core is in the western part of the channel pushed against the Yucatan slope. In other years, the core is shifted toward the center of the channel, which is similar to the observed behavior of the meandering flow reported by Abascal et al. (2003). Countercurrents in the simulation are represented by two cells near the eastern side of the channel and are in agreement with the observation by Abascal et al. (2003) that the near-surface Cuban Countercurrent is the most intense southward flow. The deeper outflow lies between ~600 m and the bottom. In the model, intensification and weakening of the simulated flow in the upper layers coincide with flow changes in the deep layers (Fig. 2d and e). The variability of the deep Yucatan flow is essential as it is intrinsically related to the LC variability (Maul, 1977; Bunge et al., 2002). GoM-HYCOM reproduces this relationship between the LC variability and the deep flow transport (Nedbor-Gross et al., 2014).

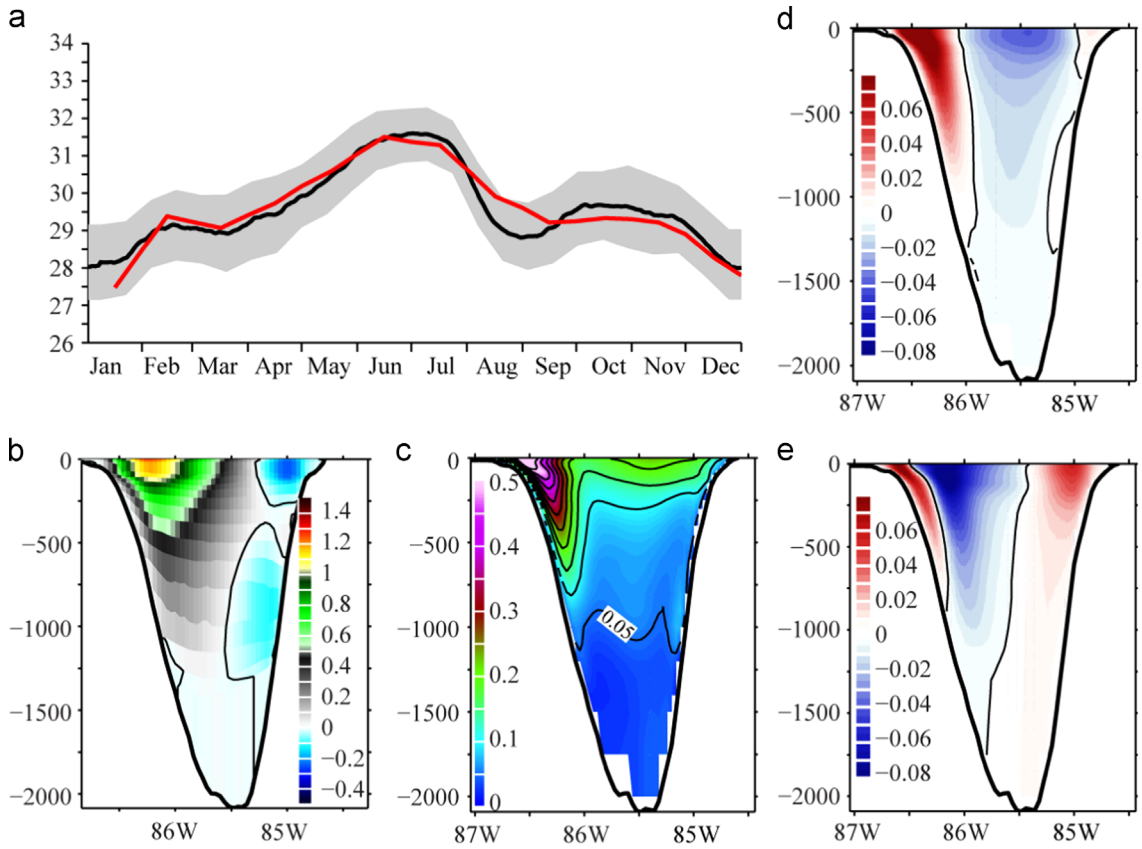

Fig. 2. Statistics of the flow in the Yucatan Channel from the 54-year GoM-HYCOM simulation: (a) the black solid line is the 2-week running average of the daily seasonal mean climatological transport (Sv) in the Yucatan Channel. The gray area encloses the 10th through 90th percentiles of the mean transport calculated using the 54 values for each year day. The red line is the bi-weekly net volume flux at the open boundaries in the Caribbean Sea. (b, c) Mean and standard deviation of along-channel velocity component (positive northward) in the Yucatan Channel (at 22°N). The standard deviation contours are shown at 0.05 interval starting from 0.05 m/s. The ordinate is depth (m). (d, e) The first two EOF modes (EOF-1 explains 62% of the variance and EOF-2 13%) of the along-channel flow. In (b, d, and e) the 0 contours are shown. (For interpretation of the references to color in this figure legend, the reader is referred to the web version of this article.)

2.2. *Automated tracking of the Loop Current front*

Since the LC and its associated LCEs are approximately in geostrophic balance, fixed SSH contour levels will very nearly follow streamlines in the flow. Past studies have used SSH contours for tracking of the LC front in SSH fields assuming that the LC front coincides with a single streamline. Other LC tracking methods have also been proposed (e.g., Andrade-Canto et al., 2013; Lindo-Atichati et al., 2013), and each yields somewhat different results. Thus, metrics for describing LC front positions vary depending on the method used to identify the front. Two techniques are used herein to evaluate the impact of different tracking techniques on LC metrics: simple tracking of an SSH contour and a more sophisticated tracking technique using Kalman filtering of SSH and SSH gradient fields.

2.2.1. *Tracking of an SSH contour*

Following Leben (2005), the LC and LCE fronts are tracked using the 0.17-m contour in demeaned SSH fields as the most basic and simple, yet reliable, LC tracking technique. Demeaned fields are calculated by subtracting the spatial mean from each daily SSH field, which is necessary to remove bias in the surface elevation fields associated with different reference surfaces and seasonal height variations due to upper-ocean warming and cooling (see Appendix A for further clarification of mean and demeaned SSH fields). Objectively, the detachment of an LCE from the LC is said to occur when the 0.17-m LC contour "breaks," resulting in two separate contours, the first defining the LC and the second defining a now detached and possibly separated LCE. Each LCE is tracked through the time series until it either dissipates or reattaches to the LC. Events in which eddies detach and ultimately reattach to the LC are called detachment events, whereas events where eddies detach and ultimately dissipate while separated from the LC are identified as separation events. The date of each LCE detachment or separation event is the date that the 0.17-m LC tracking contour breaks (Leben, 2005).

Satellite sampling limits the smallest LCEs that can be detected using altimetry; therefore eddies originating from the LC are counted as LCE separation events only if their initial areas upon separation are greater than 4000 km^2 or about 75 km in diameter. This criteria eliminates minor anticyclonic frontal eddies on the margin of the LC that typically dissipate in less than a month after separation with little or no westward propagation and have little or no impact on the recirculation trapped within the LC. These minor eddies are about half the size of the smallest LCE identified in the multi-satellite observational record to date, which was 7596 km^2 in areal extent at the time of separation (LCE Brazos, 23, Table 2). It is reasonable to assume that smaller LCEs might be observed or be found in a realistic model simulation. The 4000 km^2 criterion allows for this possibility while preventing the miscounting of small anticyclonic eddies as LCEs that are formed from warm surface water filaments on the periphery of the LC.

2.2.2. *Kalman filtering tracking*

Tracking the LC is complicated by the lack of agreement on the definition of the LC front. The LC can be defined by applying any algorithm employed for identification and tracking of mesoscale structures in the ocean except for those based on geometric criteria

Table 2
Loop Current Eddy separation events from the altimetric record: 1 January 1993 through 31 December 2010.

LCE number	Separation date	Separation period (months)	Eddy name[a]	Area (km^2)
1	10 Jul 1993	–	Whopper	24,271
2	11 Sep 1993	2.1	Xtra	43,199
3	26 Aug 1994	11.5	Yucatan	37,442
4	19 Apr 1995	7.8	Zapp	19,964
5	07 Sep 1995	4.6	Aggie	24,998
6	15 Mar 1996	6.2	Biloxi	21,530
7	25 Oct 1996	7.4	Creole	35,065
8	30 Sep 1997	11.2	El Dorado	57,751
9	22 Mar 1998	5.7	Fourchon	92,026
10	28 Sep 1999	18.2	Juggernaut	45,049
11	10 Apr 2001	18.4	Millenium	44,392
12	28 Feb 2002	10.6	Pelagic	22,137
13	13 Mar 2002	0.4	Quick	48,786
14	05 Aug 2003	16.8	Sargassum	21,318
15	08 Feb 2004	6.1	Titanic	22,511
16	26 Aug 2004	6.6	Ulysses	67,989
17	13 Sep 2005	12.6	Vortex	23,563
18	08 Feb 2006	4.9	Walker	12,421
19	04 Mar 2006	0.8	Xtreme	18,682
20	26 Sep 2006	6.8	Yankee	49,672
21	07 Jun 2007	8.3	Zorro	12,369
22	16 Nov 2007	5.3	Albert	31,304
23	06 Mar 2008	3.6	Brazos	7596
24	01 Jul 2008	3.8	Cameron	25,036
25	24 Feb 2009	7.8	Darwin	52,058
26	29 Aug 2009	6.1	Ekman	70,659
27	28 Sep 2010	13.0	Franklin	15,451

[a] Eddy names adopted from Horizon Marine www.horizonmarine.com/loop_current_eddies.php.

that have been developed specifically for closed-contour features such as eddies (e.g., the "curvature center method" (de Leeuw and Post, 1995); the "winding-angle method" (Sadarjoen and Post, 2000); the "threshold-free identification method" (Chelton et al., 2011)). As discussed in the previous section, the 0.17-m threshold for LC identification seems to be natural because under the assumption of geostrophic balance, the SSH contours are streamlines of the instantaneous geostrophic flow. At the same time, it is not obvious that one particular SSH contour can precisely follow the LC front, especially in light of the fact that the pathline of a fluid parcel can cross streamlines in a time dependent flow field. This implies a possibility of discrepancies in LC metrics derived from different definitions of the LC front. In order to test the sensitivity of LC statistics to alternate definitions of the LC front, the LC is also tracked using a discrete Kalman Filtering algorithm (Kalman, 1960) that identifies frontal positions using a combined analysis of SSH and SSH gradient fields. This provides an alternative frontal definition to those determined using only SSH fields and the SSH tracking contour method described previously (see Section 3.3 for comparison between the 0.17-m and Kalman Filtering fronts).

In the Kalman Filtering LC tracking algorithm, the supposition is made that the LC front closely follows the high-velocity core of the LC. Under a geostrophic assumption, the maximum gradient of the SSH closely follows the core of the LC and thus should be a more natural candidate to use as a criterion for eddy identification. In the following tracking methodology, the LC is defined employing the discrete Kalman Filtering algorithm (Kalman, 1960) to obtain the frontal position from two model fields (see details in Appendix B and its associated Fig. B1). Two model fields provide information for an *a priori* estimate and correction (referenced as a "measurement" in the traditional application of correcting model prediction) to obtain the final frontal location (*a posteriori* estimate). In this application, the SSH field provides the first guess of the LC front location (*a priori* estimate). The second field is the SSH gradient. The gradient field renders the information about the dynamics of the upper ocean and is used as a reference field to correct the first-guess approximation of the LC front from the SSH field. In theory, following the maximum gradient would delineate the location of the core and frontal position of the LC. However, the SSH gradient field, as with many dynamic fields, has local extrema and cannot be objectively tracked to draw a single continuous contour from the Yucatan Channel to the Straits of Florida. This algorithm uses information about the LC location from two fields, "deciding" at every step whether to trust the first or the second field more. Any other oceanographic field capable of capturing mesoscale structures can be used as a "measurement." For instance, the relative vorticity or Okubo–Weiss fields could be potential alternatives as both highlight dynamical fronts. The SSH gradient fields have been chosen to demonstrate the utility of extra information derived from the original SSH field that may be derived from satellite observations.

2.3. Simulated satellite altimetry and data processing

The impact of satellite sampling and altimeter data processing is assessed using simulated single-satellite and multi-satellite nadir sampling of the model fields and processing of the simulated along-track data into gridded SSH fields. The processing is based on the software currently used to produce the Colorado Center for Astrodynamics Research (CCAR) GoM gridded SSH product (Leben et al., 2002). Gridded products for the GoM can also be obtained from AVISO based on the processing developed by the Collecte Localization Satellites (CLS) as a part of the Developing Use of Altimetry for Climate Studies (DUACS) project; however, there are significant differences between CCAR and AVISO SSH products and results from the simulation and sensitivity tests in this study strictly apply only to CCAR altimetric analyses.

Satellite altimeter sampling is simulated by interpolating the modeled SSH anomaly fields (relative to the 54-year model mean field) along the nominal once-per-second ground tracks used by CCAR for processing of satellite altimeter data. Along-track 1-Hz SSHA measurements are simulated for exact repeat orbit ground tracks sampled by the Envisat (35-day repeat), Geosat (17-day repeat), nominal Topex (10-day repeat) and Topex interleaved (10-day repeat) satellite missions. Phasing of the Envisat, Geosat, and the nominal Topex repeat ground tracks is arbitrary and for convenience the start of the sampling along the reference ground tracks coincides with the start of the 54-year model simulation. The Topex interleaved ground track (hereafter referred to as Topex2), which is midway between and next to the nominal Topex ground track, is phased to be one half repeat period (approximately 5 days) apart in time relative to the Topex sampling. This corresponds to the configuration of the tandem satellite sampling during the Jason-2/Jason-1 tandem mission from January 2009 to April 2012 (Dibarboure et al., 2011). The interpolated along track SSH anomalies, which mimic satellite altimeter measurements referenced to a mean sea surface, are used to construct simulated SSH anomaly fields using CCAR along track processing and objective analysis procedures referenced in Appendix C. Objectively analyzed SSHA datasets have been created for sampling scenarios based on single satellite (Envisat, Geosat, Topex, Topex2) and multi-satellite (Topex–Envisat, Topex–Topex2, and Topex–Topex2–Geosat–Envisat) sampling. Processed SSH datasets for each of these sampling scenarios are recovered by adding back the 54-year GoM-HYCOM mean SSH field to the gridded SSHA datasets, which assumes perfect knowledge of the mean dynamic topography in the simulated altimetric datasets.

2.4. Mean reference SSH fields

Much of the LC SSH signal is continuous in time and cannot be directly observed in SSH anomaly; therefore, LC statistics derived

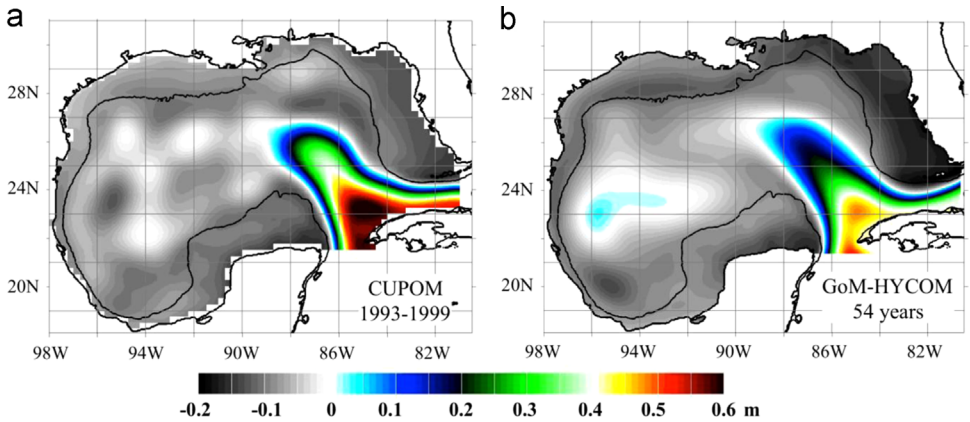

Fig. 3. Time average demeaned SSH fields (m) estimated from (a) 1993–1999 data assimilative CUPOM hindcast (Nowlin et al., 2001; Kantha et al., 2005) and (b) the 54-year GoM-HYCOM simulation. The black contours are the coastline and the 200-m isobath.

Table 3
Satellite altimeter missions used in the study.

Satellite	Launch date	Agency	Repeat period (days)	Crosstrack spacing[a] (km)
ERS-1		ESA	35	282
TOPEX/Poseidon	10 Sep 1992	NASA/CNES	10	282
ERS-2	21 Apr 1995	ESA	35	71
Geosat Follow-On	10 Feb 1998	U.S. Navy	17	147
Jason-1	18 Dec 1999	NASA/CNES	10	285
Envisat	1 Mar 2002	ESA	35	71
OSTM/Jason-2	20 June 2008	NASA		
Tandem/Interleaved Mission: 20 Sep 2000–6 Jan 2006				
TOPEX/Poseidon and Jason-1 Interleaved			10	141
Tandem/Interleaved Mission: Jan 2009–12 Apr 2012				
Jason-1 and OSTM/Jason-1 Interleaved			10	141

[a] At 26.5°N.

from satellite altimetry are based on total SSH fields estimated by adding to altimeter-derived SSHA fields a mean SSH field representative of the GoM mean dynamic topography over the time period to which the SSH anomaly is referenced. In the CCAR data product, the CUPOM 1993–1999 mean SSH (Fig. 3a) is added to SSH anomaly fields for LC tracking. This mean is based on a 7-year GoM SSH time series from an altimeter data assimilation hindcast experiment described in Kantha et al. (2005). Although this mean surface has been qualitatively validated and extensively used for over a decade for altimetric LC monitoring, the actual error in the mean SSH field remains unknown. In order to test the sensitivity of LC tracking and statistics to errors in the mean SSH field, the CUPOM mean sea surface is substituted for the 54-year GoM-HYCOM temporal mean SSH field (Fig. 3b) in the model SSH dataset (Section 3.4).

3. Results

LC variability derived from the 18-year CCAR SSH dataset is presented and compared to the LC statistics derived from the 54-year GoM-HYCOM simulation. Uncertainty of the LC metrics is analyzed from tests that assess sensitivity of the LC statistics to (1) the definition of the LC front; (2) the mean reference surface; and (3) satellite sampling. Basic benchmarks of LC variability used for evaluating of the sensitivity tests are the northernmost and westernmost positions of the Loop Current (LC extension), LCE separation period, and the relationship between the LC retreat latitude (northernmost point of LC immediately after eddy separation) and the subsequent eddy separation period.

3.1. LC metrics: satellite altimetry

This section presents LC metric statistics and analyses based on the tracking of a fixed SSH contour (Section 2.2.1) derived from the 18-year CCAR SSH dataset (1993–2010). This dataset is based on CCAR processing (Appendix C) and the multi-satellite altimetric time series available during that time period (Table 3). In the following section (Section 3.2), these altimeter-derived statistics are directly compared with statistics derived from the 54-year GoM-HYCOM simulation.

3.1.1. LC extension

The histogram of the altimeter-derived LC northernmost latitude reveals a non-unimodal distribution (Fig. 4a). The dip test of unimodality (Hartigan and Hartigan, 1985) confirms that the probability density function (PDF) of the LC northern position is not unimodal. A kernel probability density estimate (Rice, 1995) (Fig. 4a black curve) is constructed using LC northern latitude and a normally distributed density kernel with a standard deviation of 0.158. Two peaks are found in the smoothed PDF, which closely follows the two peaks (modes) in the histogram. Thus, the observed LC northern extent follows a bimodal distribution with a major mode centered on the 26.5–26.75°N bin and a minor mode centered on the 24.5–24.75°N bin.

The bimodality of the distribution of the LC northern extent indicates that there are two most common positions of the LC: the

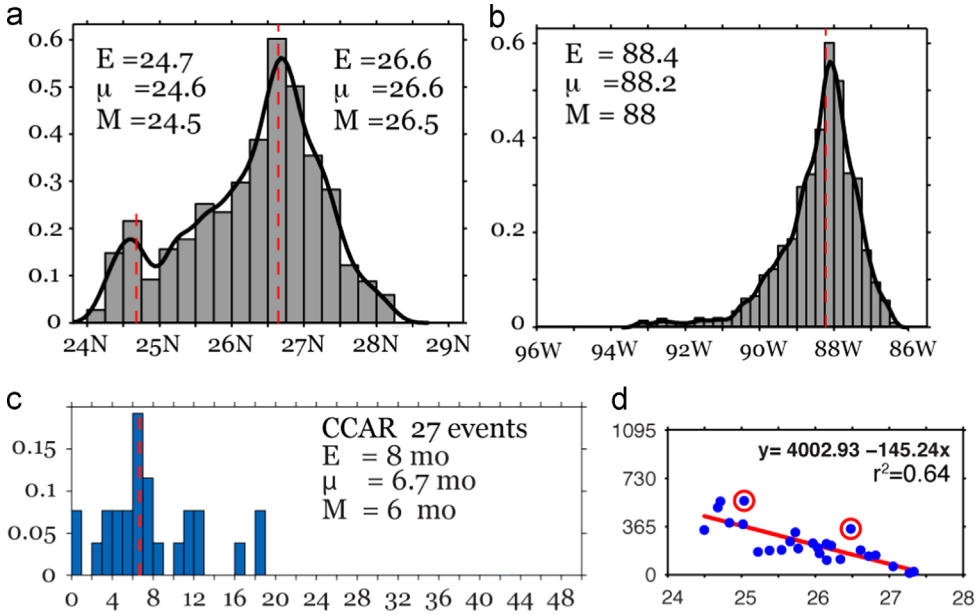

Fig. 4. The LC statistical characteristics derived from the altimeter-derived data (CCAR SSH fields): (a) normalized histogram of LC northernmost latitude and (b) normalized histogram of LC westernmost longitude (for the cases when the northernmost position is north of 25.5°N). In (a) and (b), the black curve is a kernel density estimate. The bin size is 0.25° and the vertical axis is the normalized frequency (multiplied by the bin size, it gives the occurrence probability of the LC front within the bin's longitude or latitude range). The red dashed lines are medians. (c) Normalized histograms of the LCE separation period from altimetry. Estimates of the mean (E), median (μ), and mode (M) are listed. The vertical red dashed line is the median. The ordinate is normalized frequency. (d) Scatter plot of separation period (ordinate, days) versus the retreat latitude of the LC (abscissa, degrees) following the previous eddy separation from CCAR SSH fields derived from altimeter observations. The red line is the least squares fit to the data. The red circles are outliers defined from the residual analysis. The regression and coefficient of determination (r^2) for the regression model are listed. The independent variable (x) is retreat latitude, and the dependent variable (y) is separation period in days. (For interpretation of the references to color in this figure legend, the reader is referred to the web version of this article.)

extended and retracted phases. A bimodal distribution can be approximated as a mixture of two normal distributions centered around two modes (Schilling et al., 2002). Estimated characteristics of these distributions are listed in Fig. 4a. The data suggest that the most common northern location of the LC front lies within 24.5–24.75°N when the LC is in a retracted phase. When it is extended, the LC northern location is predominantly within 26.5–26.75°N.

3.1.2. Separation period and the retreat latitude of the Loop Current

Analysis of the altimeter-derived SSH gridded fields for the 18-year period from 1993 through 2010 identified a total of 27 LCE separation events (Table 2). The mean eddy separation period is 8 months, the median is 6.7 months, and the mode is 6 months. A normalized histogram (the total area equals 1) of the LCE separation periods from satellite observations (Fig. 4c) reveals an asymmetric, positively skewed distribution of the data.

Leben (2005) first reported the relationship between the LC retreat latitude, defined as the northernmost point of the LC immediately after eddy separation, and the subsequent eddy separation period. LC statistics derived from altimetry-based SSH fields (using altimeter records from 1993 to 2003) revealed a linear relationship between the retreat latitude and the separation period. This relationship shows that the separation period will be longer when the LC retreats farther south after eddy separation. The relationship still holds for the updated altimeter data extending to 2010 (Fig. 4d). A regression fit with a coefficient of determination of 0.63 indicates a robust linear relationship between the separation period and the retreat latitude of the LC. This result indicates some regularity in the LC behavior in support of the ideas advanced by Lugo-Fernandez (2007) regarding predictability of the LC system and by Lugo-Fernandez and Leben (2010) regarding the prediction of the time until eddy separation during an incipient LC intrusion. Nevertheless, the relationship is not perfectly linear. There are notable deviations about the linear fit. For instance, there is a wide spread of observed separation periods, from about 6 months to 18 months, for LC retreat latitudes near 25°N.

3.2. LC metrics: GoM-HYCOM

This section presents LC metric statistics and analyses based on the tracking of the 0.17-m SSH contour (Section 2.2.1) derived from the 54-year GoM-HYCOM simulation. These LC statistics derived from GoM-HYCOM based on the 0.17-m SSH contour will be referred as "original" statistics in the following sections on sensitivity tests.

3.2.1. LC extension

The distribution of the northern extent of the LC from the model (Fig. 5a) has some similar features as the distribution of the altimeter-based metric (Fig. 4a), but with notable differences. Although both distributions are bimodal, the distribution of the model data is strongly bimodal. It has two well-defined modes. One mode is in the 24.5–24.75°N bin, and the second mode is in the 27.0–27.25°N bin. In the simulation, the LC northern extent is farther north during both retracted and extended phases compared to the altimeter-based data. The most striking difference between the distributions of the LC northern extent from GoM-HYCOM and altimeter-derived data is the higher probability of the LC to be in the retracted position in the model experiment. The probability of the LC to be south of 25.5°N is 0.38 for GoM-HYCOM and 0.2 for CCAR data.

The distributions of the maximum western longitude of the LC in the model (Fig. 5b) and altimeter-derived data have similar statistics: mean (88.4°W), mode (88–88.25°W), and median (88.2°W). The model predicts the LC front as far west as 95°W during episodic extreme western intrusion events when several small LCEs are enclosed by a single 0.17-m contour. Similar extreme LC intrusion events have been recorded in altimeter observations. For example, two LC eddies separated within a two-week interval in February and March 2002 (Table 3) and were identified by Horizon Marine Inc. as

Pelagic and Quick (www.horizonmarine.com/loop_current_eddies.php). Before these eddies separated, the westernmost extent of the LC was ~93.1°W.

3.2.2. LC eddy separation period

LC metrics are computed from the model SSH fields employing the LC tracking algorithm identical to that used to obtain metrics from the altimeter-based data. A total of 69 LCE separation events in the 54-year model run are identified. There is a general agreement in the distributions of the LCE separation period derived from GoM-HYCOM and CCAR SSH data. Normalized histograms of the LCE separation periods from the model (Fig. 5c) reveal asymmetric, positively skewed distribution of the data, similar to the altimeter-derived results (Fig. 4c). The model histogram has a longer tail due to a single 4-year separation interval simulated in the model as well as several events with a separation interval longer than 18 months, the longest LCE separation interval observed in the altimeter-based data (1993–2010). The mean separation period from the model is 9.3 months, the median is 6.1 months, and the mode is 6 months.

3.2.3. Separation period and the retreat latitude of the loop current

The least-squares fit to the separation period and retreat latitude data from the 54-year GoM-HYCOM (Fig. 5d) has a slope similar to the linear regression derived from observations (Fig. 4d). The regression is calculated without the 4-year separation period, which is an obvious outlier and an influential point (Jennrich, 1995). The model reproduces the relationship found in CCAR data: when the LC retreats farther south after an eddy shedding, the subsequent separation period will be longer. The coefficient of determination for GoM-HYCOM data (0.37) is lower than the coefficient for CCAR data (0.64) implying weaker linearity in the relationship between the separation period and the retreat latitude in the model simulation. Nevertheless, an Analysis of Covariance (ANCOVA) *F*-test (Jennrich, 1995) does not indicate a statistically significant difference between the regression slopes.

3.3. Sensitivity of LC metrics to the definition of the LC front

Although the 0.17-m LC tracking contour technique was developed to be a simple and robust proxy for the high-velocity LC core

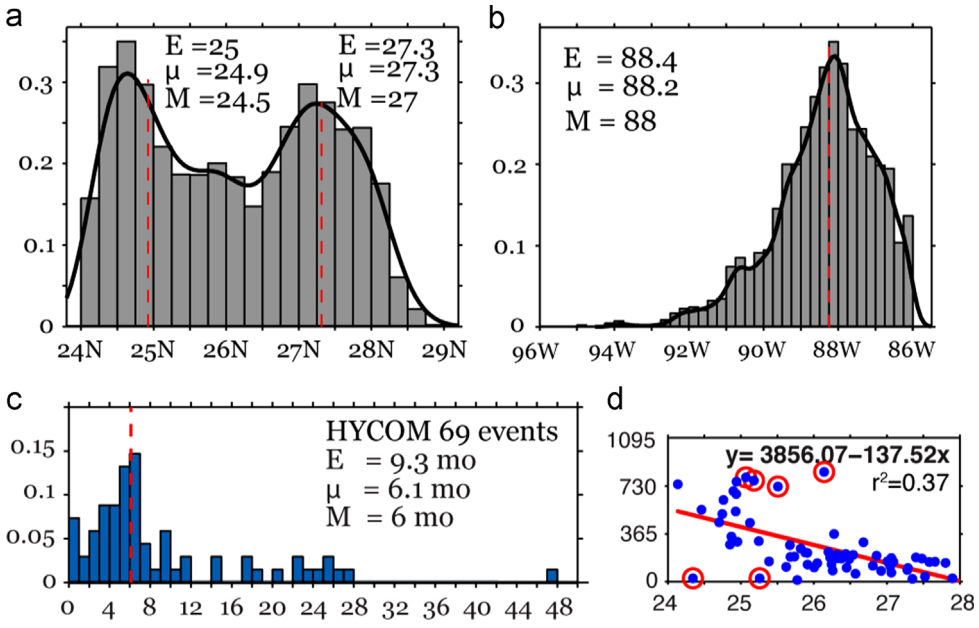

Fig. 5. Same as Fig. 4 but for GoM-HYCOM. In (d), the 4-year separation period was discarded before calculating the least squares fit.

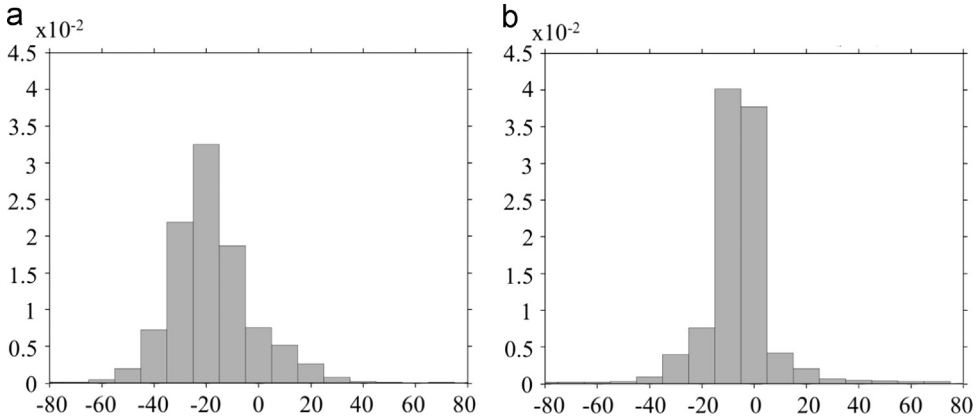

Fig. 6. Normalized histograms of the distances (km) between the LC contours and the local maximum SSH gradient: (a) LC contour defined as the 0.17-m isoline. Negative distances indicate that the maximum SSH gradient is outside the LC relative to the 0.17-m contour. Positive distances indicate the inside location of the maximum SSH gradient relative to the 0.17-m contour. (b) Kalman Filter-based LC tracking. Negative distances indicate that the maximum SSH gradient is outside the LC relative to the Kalman Filter-based contour.

depicted in objectively interpolated SSH maps, the contour does not necessarily coincide exactly with peak velocities within the core of the LC stream. The location of the 0.17-m contour relative to the maximum SSH gradient perpendicular to the contour, which by definition does coincide with the maximum surface geostrophic velocity within the high velocity LC core, has been estimated in GoM-HYCOM (Fig. 6a) and is consistently displaced inside of the LC relative to the location of the maximum SSH gradient. In 80% of the cases the location of the maximum SSH gradient is in the range from −35 km to −5 km (negative indicates displacements toward the outside the LC) relative to the 0.17-m tracking contour, consistent with previous estimates of this offset based on comparisons of CCAR altimetry product with SST and industry frontal analyses (Leben, 2005; Forristall et al., 2010). Therefore, it is important to determine how LC characteristics would change if a tracking method with the ability to more closely track the high velocity LC core were employed.

In order to test the sensitivity of the LC statistics to an alternate SSH-based frontal definition, the LC core defined using the Kalman Filtering algorithm is compared to the 0.17-m threshold definition. In the modeled SSH fields, this approach more skillfully tracks the LC core (maximum SSH gradient). In 80% cases, the distance between the Kalman Filter-based tracking and the maximum SSH gradient is in the range from −15 km to 5 km (Fig. 6b). Nevertheless, most of the time, the LC front identified by the Kalman Filter-based method only slightly deviates from the 0.17-m original contour (Fig. 7a or animation). However, timing of the LCE detachment–reattachment may differ by several days (1–3 days) depending on the tracking method (Fig. 7b; in the animation: detachment events in early April, late May, late June, middle August). In Fig. 7b (corresponds to the animation frame dated as "1993/6/26") the original 0.17-m contour ("Orig. GoM-HYCOM") delineates the LC in the retracted stage after a big eddy has been shed. At the same time, the Kalman Filter contour still includes the eddy in the LC indicating that the eddy has not detached yet. Statistics of the maximum northern and western extents of the LC derived from the new definition of the LC changed slightly (Fig. 8a and b), compared to the original estimates (Fig. 5a and b).

The LC and LCEs identified by the Kalman Filter algorithm are larger than those tracked by the 0.17-m contour. The area threshold value used to identify the LCE separation (Section 2.4) has been adjusted to take into account the increased areal extent. Although the majority of the LCEs identified by the Kalman Filter-based method are the same eddies defined by the 0.17-m contours, several eddies tracked by the 0.17-m contour and identified as LCEs have not been tracked by the KF and vise versa. These eddies are small anticyclones (close to the threshold value) shed from the northwestern side of the LC during its extreme northward extension. The probability density functions of the LCE separation periods (Figs. 4c and 8c) are alike in general but have discrepancies in detail. Nevertheless the Kolmogorov–Smirnov test (Massey, 1951) does not reject the hypothesis that the two distributions are the same. With the Kalman Filter-based definition of the LC, the mean (9.4 months) and the median (6.2) separation periods are close to the tracking approach based on the 0.17-m contour (9.3 and 6.1 months, respectively).

The relationship between the separation period and the retreat latitude of the LC defined based on the Kalman Filter technique (Fig. 8d) is qualitatively similar to the original relationship from GoM-HYCOM (Fig. 5d). The regression slope (−137.5) is almost the same as estimated from the GoM-HYCOM using the 0.17-m SSH contour LC tracking approach.

These results demonstrate that the alternative definition of the LC front has not significantly impacted the statistical description of the LC behavior. In the remainder of the paper we will use the LC tracking technique based on the 0.17-m SSH contour to evaluate the uncertainty of LC statistics.

3.4. Sensitivity of the LC statistics to the mean reference surface

The calculation of LC statistics from altimeter observations is based on total SSH fields obtained by adding the CUPOM mean field as a reference field (Fig. 3a) to gridded altimeter SSH anomaly fields (Section 2.3). To test the sensitivity of the LC tracking and statistics to errors in the reference SSH field, the following experiment (hereafter the "CUPOM experiment") is conducted. The 54-year GoM-HYCOM temporal mean SSH field (Fig. 3b) is subtracted from the instantaneous model SSH fields, providing anomaly fields (analogous to gridded altimeter-based SSH anomaly fields). Then, the temporal mean SSH from CUPOM (Fig. 3a) is added as a reference SSH to the anomaly fields. The resulting total SSH fields with the CUPOM mean are used to identify and track the LC using the technique presented in Section 2.4.

The calculated northern and western extensions of the LC from the original GoM-HYCOM and CUPOM experiment datasets have discrepancies, revealing some sensitivity to the systematic errors induced by the reference mean as mentioned by Leben (2005). The differences in the statistics from the two experiments stem from disparities in the LC front locations introduced by swapping GoM-HYCOM mean SSH with the CUPOM reference mean SSH field.

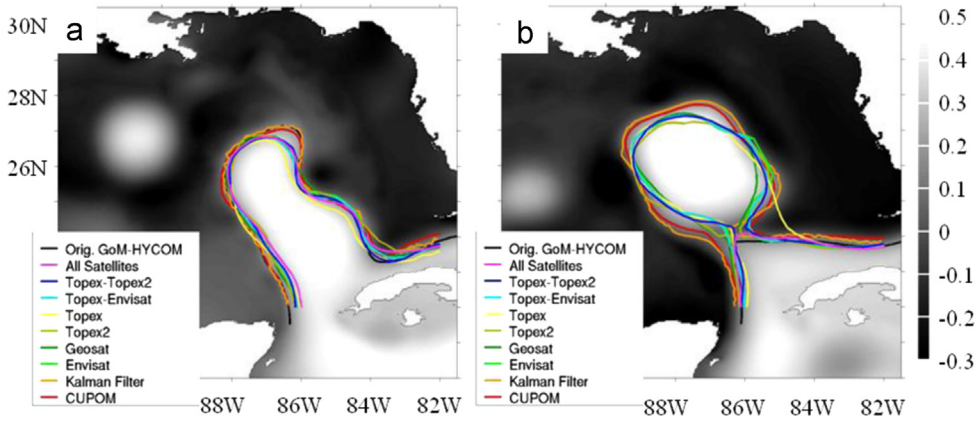

Fig. 7. (Animation in online version). Demeaned SSH fields (m) and LC contours from two separate model output times. The black contour is the LC front from the original GoM-HYCOM SSH field. The colored LC contours are obtained from the sensitivity tests where the LC location is defined by: the Kalman Filtering method (Section 2.2.2); the 0.17 m SSH anomaly contour from the original SSH field sampled into various satellite tracks and then gridded following the Leben (2005) approach (Section 2.3); the 0.17 m SSH anomaly contour from the GoM-HYCOM with the mean SSH field swapped with the CUPOM mean (Section 2.4). For the satellite track sampling experiments, the legend indicates the satellite tracks used, with "All Satellites" indicating combined tracks from Topex–Topex2–Geosat–Envisat: (a) at this model time, all LC contours demonstrate good agreement with the original LC contour. (b) LC contours show large disagreement across the sensitivity tests with the original LC contour during an LC eddy detachment.

Discrepancies in the LC front shape between GoM-HYCOM SSH fields and the CUPOM experiment SSH fields result in only small changes in the distribution of the LC northern extension (Fig. 9a). Qualitatively, the distributions in Figs. 5a and 9a are similar (see the cyan line in Fig. 9a that is the kernel density estimate for GoM-HYCOM shown in Fig. 5a). Even fewer changes are noticeable in the distribution of the LC western extension derived from the CUPOM experiment (Fig. 9b) compared to the original GoM-HYCOM (Fig. 5b). Thus, swapping the reference SSH field has had little effect on the distributions of LC extension.

The histograms of the LCE separation periods in GoM-HYCOM and the CUPOM experiment have general resemblance (Figs. 5c and 9c). The two-sample Kolmogorov–Smirnov test (Massey, 1951) cannot provide enough evidence to reject the null hypothesis that distributions of the eddy separation periods in the CUPOM experiment and original GoM-HYCOM are the same. In the CUPOM experiment several separation events were not identified resulting in a total of 65 events versus 69 in the original simulation. The difference in the number of shed eddies is explained by the sensitivity of the LC tracking methods to the definition of the LC front (Section 2.4). LC contour differences between the CUPOM experiment and the original GoM-HYCOM simulation lead to different values of LC area (Fig. 7b). Also note the different shapes of the LCEs defined by the CUPOM and original GoM-HYCOM contours before shedding events on 5/28, 6/23, 8/16 in the companion animation to this paper. Some small eddies counted in the original simulation because their areas were slightly bigger than the threshold became small enough to be discarded in the CUPOM experiment. Metrics calculated from the CUPOM experiment have slightly changed the estimates of mean (9.8 versus 9.3 months in GoM-HYCOM) and median (6.2 versus 6.1 months) separation periods. The mode has not changed (6 months).

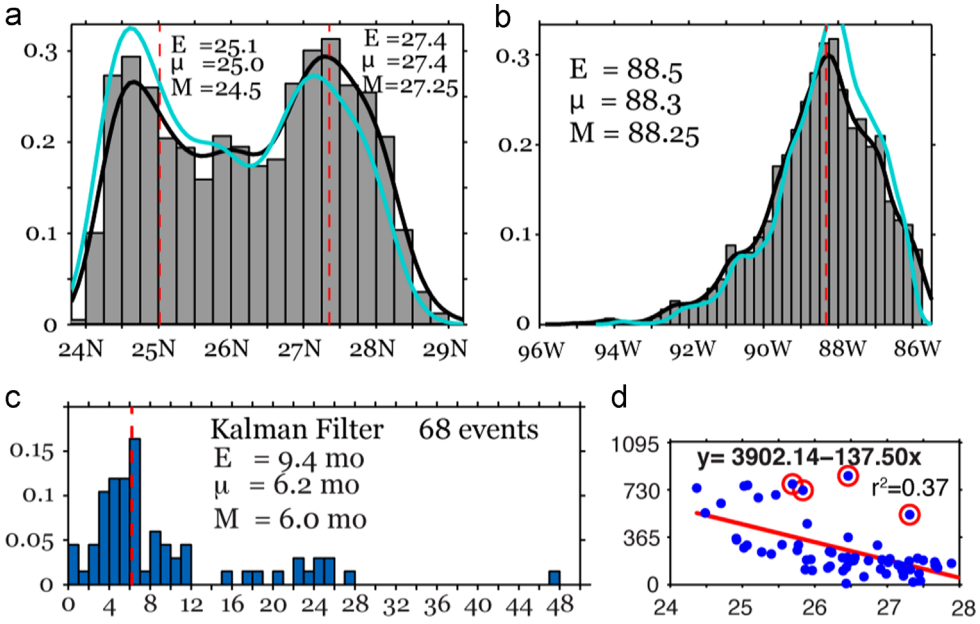

Fig. 8. Same as Fig. 5 but for the Kalman Filter-based LC tracking. In (a) and (b), the cyan curves are the kernel density estimates for GoM-HYCOM (shown in Fig. 5a and b).

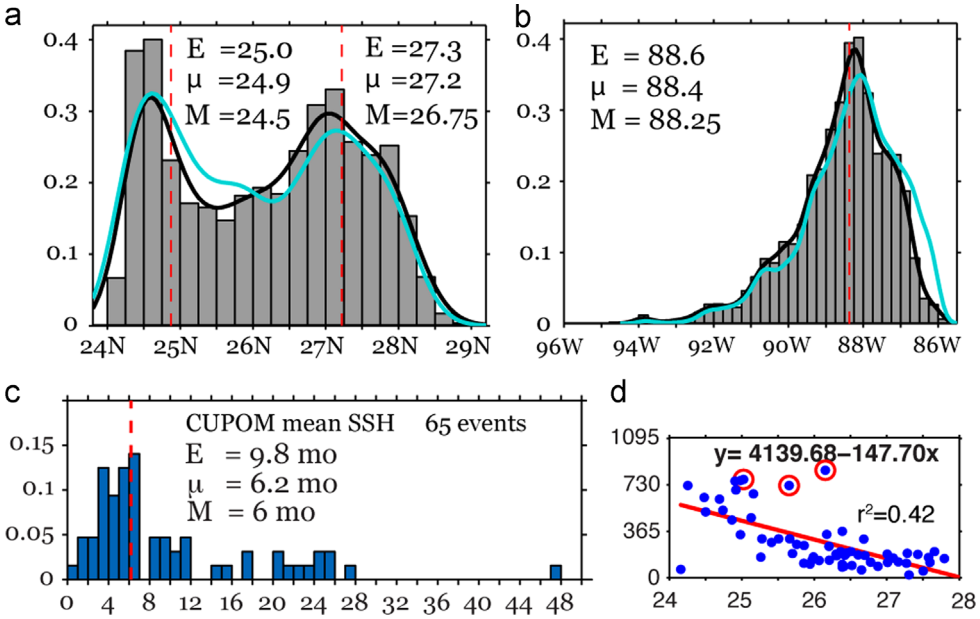

Fig. 9. Same as Fig. 5 but for the CUPOM experiment. In (a) and (b), the cyan curves are the kernel density estimates for GoM-HYCOM (shown in Fig. 5a and b).

The relationship between the separation period and the retreat latitude of the LC in the CUPOM experiment (Fig. 9d) demonstrates minor changes compared to GoM-HYCOM (Fig. 5d). The regression slope for the CUPOM experiment (− 147.7) is statistically similar to the slope in GoM-HYCOM, indicating that the retreat–separation period relationship has not changed after swapping reference SSH fields.

In summary, the choice of the mean reference SSH fields can lead to small differences in the shapes of the LC and LCEs between the CUPOM experiment and GoM-HYCOM. The most prominent impact is seen in timing of the LCE detachment–reattachment and separation events. Nevertheless, these discrepancies have minor impact on the LC and eddy shedding statistics.

3.5. Sensitivity of the LC statistics to satellite sampling

The simulated altimetric sampling of the model simulation described in Section 2.3 is used to test the sensitivity of the LC statistics to inhomogeneity of satellite altimeter sampling in space and time. Metrics are computed using the LC tracking technique based on the 0.17-m SSH contour to evaluate the uncertainty of the LC and eddy statistics.

Apparent changes in the shape of the LC extent histograms indicate that the northernmost and westernmost positions of the LC are impacted by satellite (Figs. 10 and 11). The most dramatic changes in the shape of the northernmost position histograms are observed in the Topex, Topex2, and Topex–Topex2 experiments (Fig. 7 or animation). However, all distributions retain strongly bimodal shapes, similar to GoM-HYCOM (the cyan curves in Fig. 10 are the kernel density estimates for the original GoM-HYCOM shown in Fig. 5a). It is noteworthy that, in the satellite experiments, the mean, median and mode of the LC northern latitude during the mature phase have shifted southward compared to their values in GoM-HYCOM. This indicates that the northern extents of the LC fronts derived from altimeter-based SSH fields have slight southward biases and is likely due to the along track detrending and smoothing applied to the altimeter data during the objective analysis.

Histograms of the westernmost position of the LC are more sensitive to the sampling strategy, again with the Topex, Topex2, and Topex–Topex2 experiments as outliers. The histogram for the experiment in which the model data are synthetically sampled by four satellites (Fig. 11g) has the closest resemblance to the histogram produced from analysis of the full GoM-HYCOM SSH fields (Fig. 11a). Hence, statistics of the northern- and westernmost positions of the LC show strong sensitivity to the spatial and temporal inhomogeneity of the satellite products.

The probability density functions of the LCE separation periods indicate good agreement with GoM-HYCOM (Fig. 12a) and general similarity among the satellite sampling experiments (Fig. 12b–h). The Kolmogorov–Smirnov test does not provide enough evidence that any of the probability density distributions is different from the original GoM-HYCOM. Nevertheless despite the general agreement among the shapes of the histograms, the impact of inhomogeneity of satellite observations is apparent in these distributions. Because of the varying spatial and temporal accuracy of SSH representation across selected satellite experiments, definitions of the LC frontal position differ among the experiments. This leads to differing numbers of LCE separation events (varying from 63 events in the Envisat–Geosat–Topex–Topex2 and Topex–Topex2 experiments to 69 events in the Envisat and Topex experiments) and disparate redistribution of the events in the histograms. The sample mean varies from 9.3 (Topex and Envisat) to 10.2 months (Envisat–Geosat–Topex–Topex2 and Topex–Topex2) compared to 9.3 months from the original GoM-HYCOM data. Note that the medians exhibit less sensitivity to the subsampling procedure. Statistics from the experiment with the combined four satellites still do not agree perfectly with statistics from GoM-HYCOM. The differences in separation event counts among experiments illustrates the difficulties encountered when using a fixed area criterion to count or ignore eddies.

The linear relation between the separation period and the retreat latitude of the LC reveals high sensitivity to the LC statistics from the satellite experiments (Fig. 13). The main reason is that this linear relationship is sensitive to the definition of the LC frontal location, which differs considerably across the sensitivity experiments (Figs. 10 and 11) and deviates from the original LC front in GoM-HYCOM. One noteworthy result is that the "Topex" experiment (Fig. 13d) has a weak linear relationship with the coefficient of determination of only 0.09. In this experiment, the linear relationship between the separation period and the retreat latitude is not obvious. Thus, synthetic SSH fields reconstructed

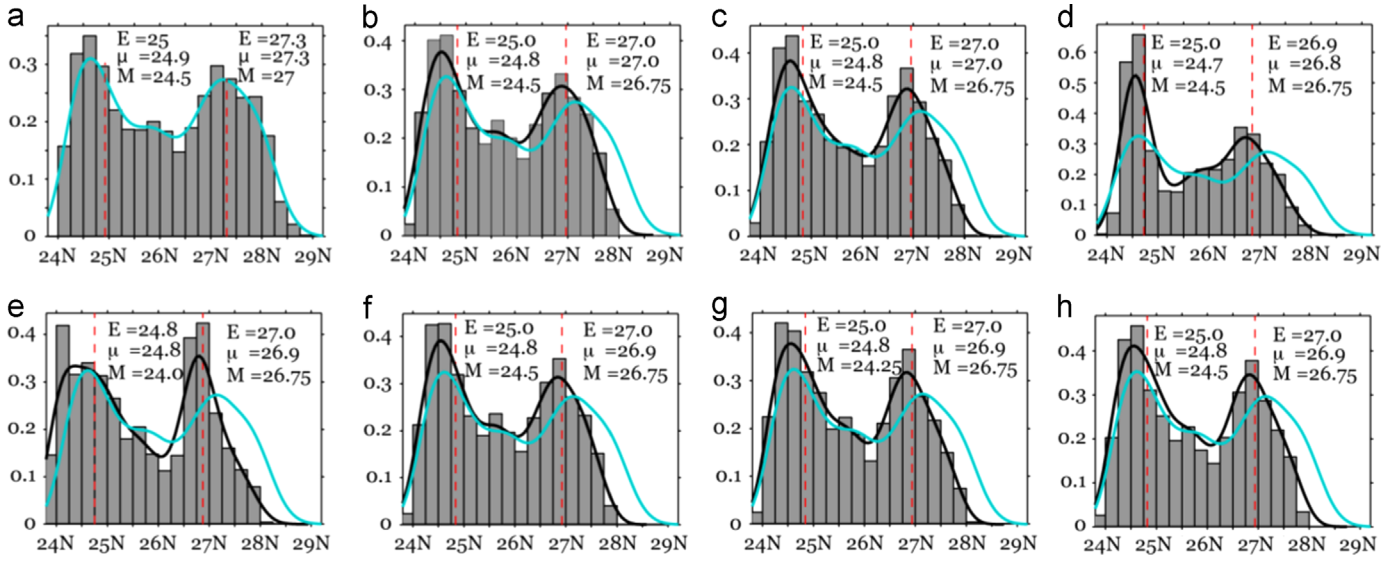

Fig. 10. Normalized histograms of the LC northern extension (°N) with 0.25° binning derived from (a) GoM-HYCOM SSH fields (replicated from Fig. 5a for ease of comparison); HYCOM SSH fields interpolated into satellite tracks (b) Envisat; (c) Geosat; (d) Topex; (e) Topex2; (f) Topex–Envisat; (g) Topex–Topex2; and (h) Topex–Topex2–Geosat–Envisat. Vertical dashed lines are medians. Estimates of the mean (E), median (μ), and mode (M) for individual distributions of the bimodal pdfs are presented. The vertical axis is the occurrence probability. The cyan line is the the kernel density estimate for GoM-HYCOM. The black lines are the kernel density estimates for the interpolated SSH fields from simulated satellite sampling and data processing.

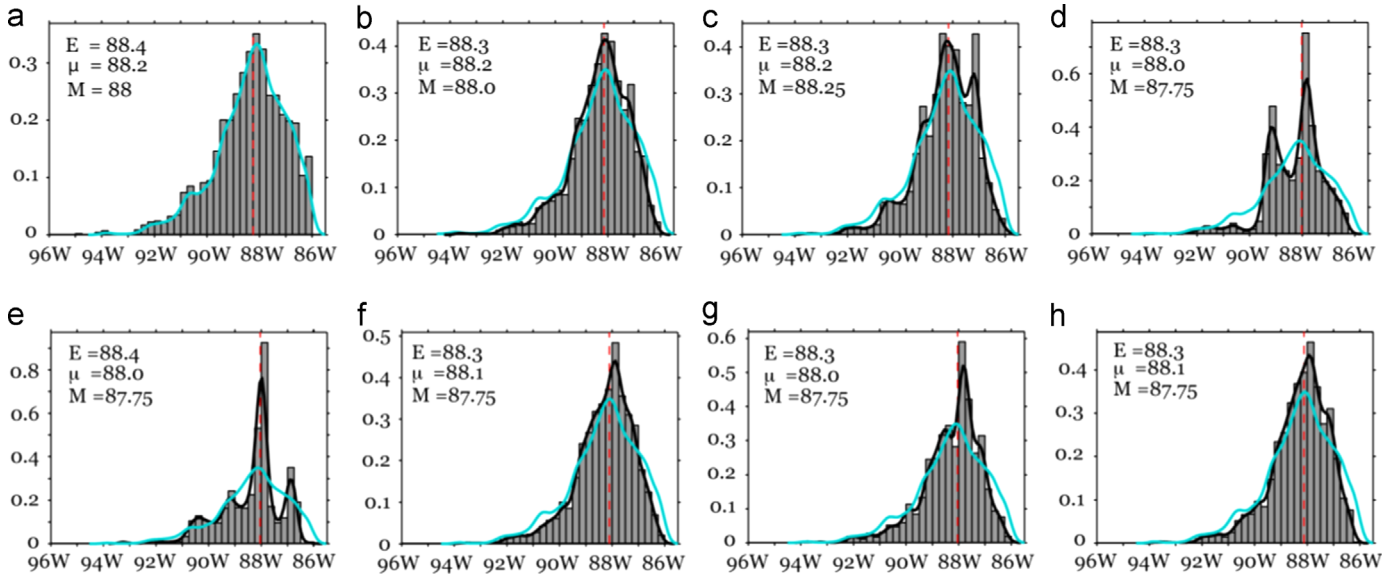

Fig. 11. Normalized histograms of the LC western extension (°W) with 0.25° binning derived from (a) GoM-HYCOM SSH fields (replicated from Fig. 5b for ease of comparison); HYCOM SSH fields interpolated into satellite tracks (b) Envisat; (c) Geosat; (d) Topex; (e) Topex2; (f) Topex–Envisat; (g) Topex–Topex2; and (h) Topex–Topex2–Geosat–Envisat. Other notations are similar to Fig. 10.

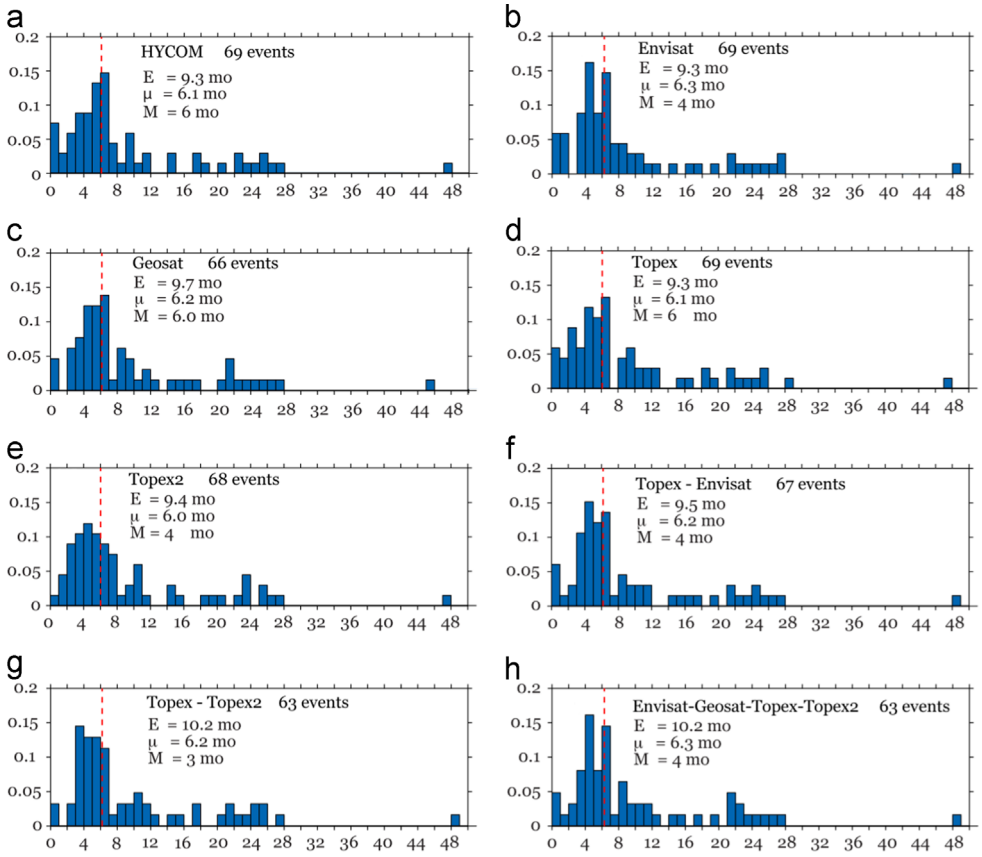

Fig. 12. Normalized histograms of the LC eddy separation period (months) with 1-month binning. LCE separation dates are derived from (a) GoM-HYCOM fields (replicated from Fig. 5c); HYCOM SSH fields interpolated into satellite tracks (b) Envisat; (c) Geosat; (d) Topex; (e) Topex2; (f) Topex–Envisat; (g) Topex–Topex2; and (h) Topex–Topex2–Geosat–Envisat.

from GoM-HYCOM SSH anomalies interpolated onto the satellites' tracks show that the shape and intensity of mesoscale features is distorted by the satellite sampling and data processing, impacting the LC metrics. Nevertheless, an important conclusion is that the LC metrics and statistics calculated from the synthetic SSH fields are close to those calculated from the original GoM-HYCOM SSH fields except for the separation period – retreat latitude relationship.

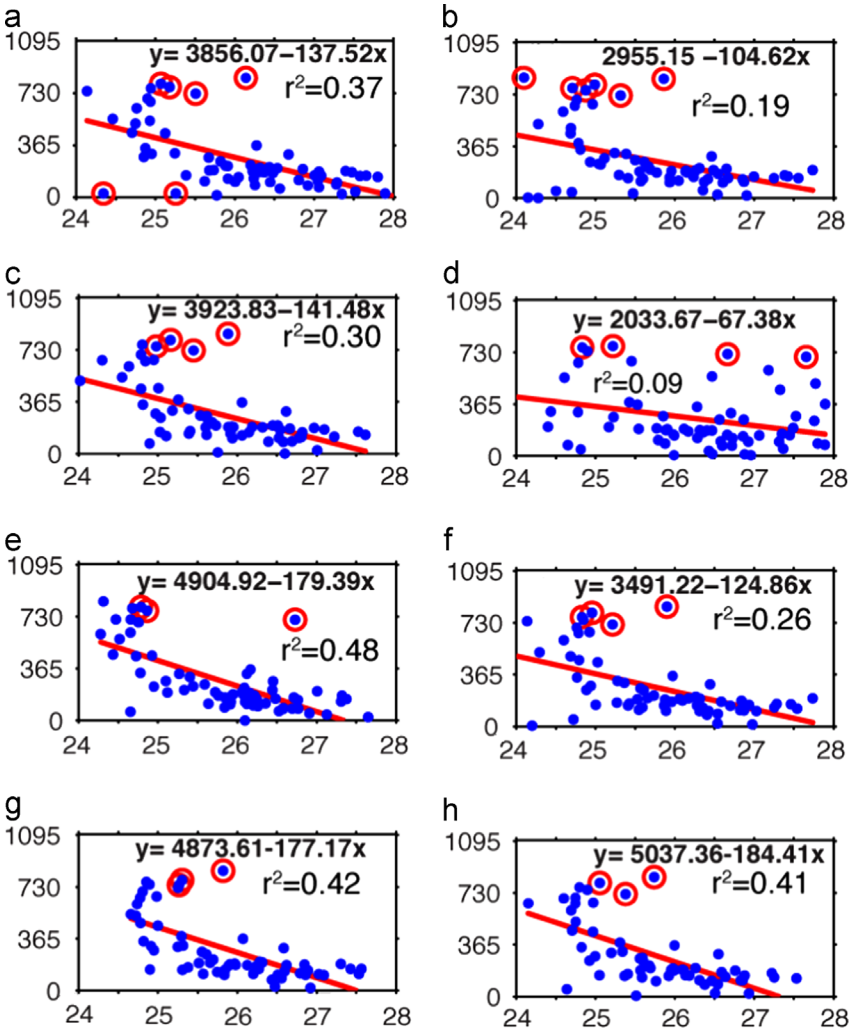

Fig. 13. Scatter plot of separation period (ordinate) in days versus the retreat latitude of the LC (abscissa) following the previous eddy separation from the sensitivity tests: (a) GoM-HYCOM (replicated from Fig. 5d); Satellite experiments: (b) Envisat; (c) Geosat; (d) Topex; (e) Topex2; (f) Topex–Envisat; (g) Topex–Topex2; (h) Topex–Topex2–Geosat–Envisat. The line is the least squares fit to the data. The 4-year separation period was discarded before calculating the least squares fit. The circles are outliers defined from the residual analysis. The regression models (y is separation period in days and x is the retreat latitude) and the coefficients of determination (r^2) are listed.

4. Analysis of the LC stationarity

An important question in assessing LC variability is what record length would suffice to derive representative statistics of the system. This question is related to a long-standing debate on the regular versus irregular LC behavior and its predictability (Maul, 1977; Sturges and Evans, 1983; Sturges and Leben, 2000; Nowlin et al., 2001; Leben, 2005; Lugo-Fernandez, 2007; Lugo-Fernandez and Leben, 2010; Chang and Oey, 2013). It still remains unclear whether the LC system can be approximated as a stationary process (DiMarco et al., 2005). The answer to this question is essential for interpretation and practical application of the LC statistical characteristics. In theory, if the LC eddy separation time series is non-stationary the sample mean, variance, auto-correlation and higher moments are not well defined (Nason, 2006). In particular, the mean and the variance are not constant and change over time and thus, cannot be consistently estimated from a time series (von Storch and Zwiers, 1999).

Recently, changes in the mean eddy separation period and eddy separation frequency were discussed in Vukovich (2012) and Lindo-Atichati et al. (2013). Both studies reported an increase of eddy separation frequency and decrease in the LC's average separation period during the 2000s compared to estimates from an earlier time period of observations. These changes may be related to changes in the LC and indicate the non-stationary nature of the system.

One way to evaluate evidence of non-stationarity in a time series is to look how statistical estimates vary when calculated from different segments of the time series (Nason, 2006). To test this, an 8-year window (the minimum record length that provides >5 separation events per segment) is slid along the CCAR data for 1993–2010, providing 11 segments (1993–2000, 1994–2001, etc.) of individual time series of the LC front position. For each 8-year segment, the following statistics are derived: the mean and standard deviation of separation period (months), and regression parameters for eddy separation period versus retreat latitude of the LC (Fig. 14a–c). The results demonstrate noticeable variability of the LC statistics across different 8-year segments. Being inversely proportional to the number of separation events, the mean separation period ranges from ~6 to 12 months for the 8-year segments of CCAR altimetry data (Fig. 14a). Note the wide 95% confidence intervals due to the low number of the separation events during the 8-year segments. It is noteworthy that eddy separation frequency increased and the mean eddy separation period decreased (Fig. 14a) over the last decade (segments 2000–2007, 2001–2008, 2002–2009, and 2003–2010), in agreement with Vukovich (2012) and Lindo-Atichati et al. (2013).

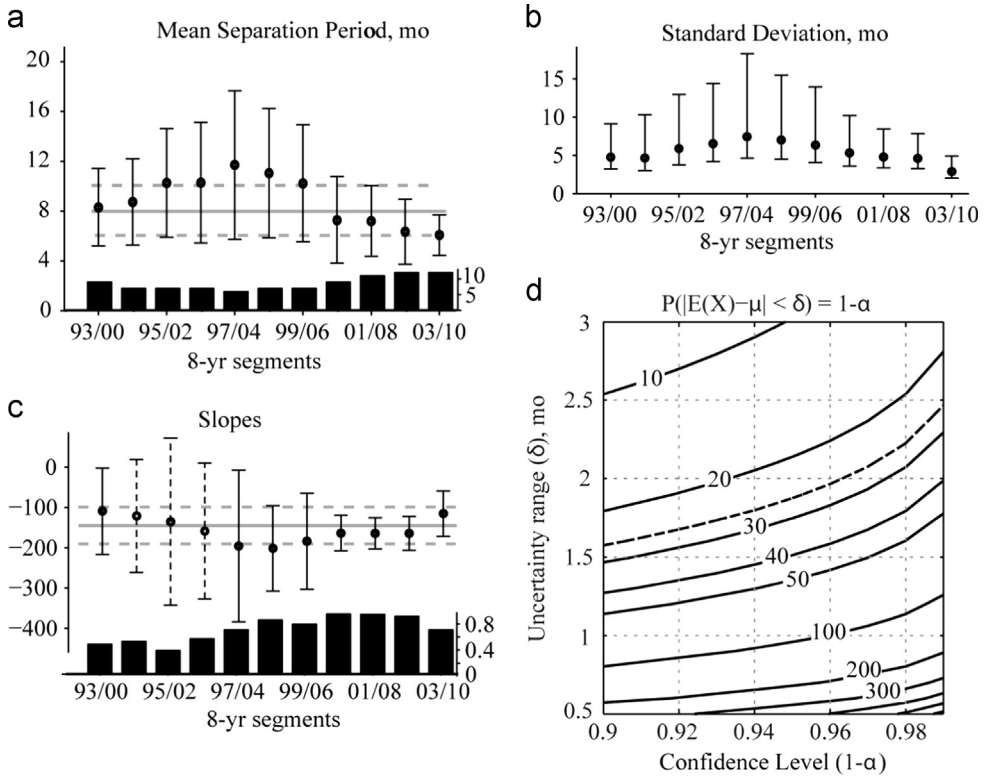

Fig. 14. (a–c) LC statistics for overlapping 8-year segments of the altimeter-derived data (CCAR SSH fields) for 1993–2010. The numbers on the horizontal axis are years of every other time segment: (a) mean separation period estimates (months) are shown with the black circles for each segment. The vertical lines are the 95% confidence intervals for the mean separation period. Horizontal gray solid and dashed lines are the mean separation period and the 95% confidence interval, respectively, for the entire CCAR data record. At the bottom, the bar diagram shows the number of separation events during the 8-year segments. (b) Standard deviation estimates and their 95% confidence intervals. (c) The slopes and 95% confidence intervals for the regression models of separation period versus the retreat latitude of the LC. Dashed significance bars designate statistically non-significant slopes. Horizontal gray solid and dashed lines are the slope and 95% confidence interval for the entire period of the analyzed CCAR data. At the bottom, the bar diagram presents the coefficients of determination for the regression model of separation period versus the retreat latitude of the LC following the previous eddy separation. (d) Estimated number of LC eddy separation events (contours) that is required to guarantee at $(1-\alpha)$% confidence level that the deviation of the estimated mean separation period from the true mean does not exceed δ months.

Variability of the standard deviation of the LCE separation period (Fig. 14b) mirrors the variability of its mean. The standard deviation is small at the beginning and end of the observational record and peaks for the segment 1997–2004.

The linear relationship between the separation period and the retreat latitude of the LC is not robust for all the 8-year segments (Fig. 14c). During several time intervals (1994–2001, 1995–2002, 1996–2003) the regression slopes are not statistically significant. By contrast, during the time segments 2000–2007, 2001–2008, and 2002–2009 the relationship is nearly perfectly linear with high values (>0.8) of the coefficient of determination (Fig. 14c).

Fig. 14a–c demonstrate substantial variability of the LC characteristics over the analyzed time interval, which may be an indicator of non-stationarity of the LC separation process. In order to determine whether the LC separation time series is (weakly) stationary over the altimetry record, equality of means and variances across the 8-year segments is tested. It is noteworthy that overlapping 95% confidence intervals of the individual estimates (Fig. 14a and b) do not guarantee the equality of the parameters across the groups (Payton et al., 2003; Lanzante, 2005). To test equality of the means from the 8-year segments, a one-way analysis of variance (ANOVA) procedure is used (Jennrich, 1995). The null hypothesis that is tested by the ANOVA is that all the means are the same (the *F*-test). Only non-overlapping segments can be used to comply with the independence requirement for the ANOVA *F*-test. Two non-overlapping 8-year segments in the 18-year CCAR data record are the first (1993–2000) and the last (2003–2010), and these segments are used for testing the means. The *p*-value obtained from the *F* statistic ($F_{1,\ 18}=0.26$) is 0.6 (which is greater than the significance level of 0.05) suggesting that the null hypothesis cannot be rejected. For testing equality of variances, Levene's test is used (Levene, 1960) with the null hypothesis of homoscedasticity. The *p*-value for the Levene's statistic for the first and the last 8-year segments ($F_{1,\ 18}=2\times10^{-5}$) is 0.9, which is also too high to reject the null hypothesis. Hence, both tests fail to reject the null hypotheses that the individual means and variances for first and the last 8-year segments are the same. Thus, despite obvious variability of the mean and standard deviation estimates in Fig. 14, there is not enough evidence that the parameters of the process are significantly different during the first and second halves of the satellite altimeter record undermining the hypothesis of LC non-stationarity. Analyzed observational records over 1993–2010 cannot prove that the LC separation process is non-stationary suggesting that the mean and the variance of the process are well defined and sample estimates converge to the process mean and variance as the duration of observations increases.

From the 1993 to 2010 altimetric data, the LC mean separation period is within (6.1–9.8) months at 0.05 significance level. As the number of separation events grows (i.e., increasing record length) the estimate of the mean separation period ($\overline{X}$) will converge to the process mean (μ). The Lindeberg–Levy central limit theorem is applied to estimate how "large" the number of observations needs to be to guarantee that the mean estimate deviates from the process mean no more than δ (Rice, 1995):

$$\lim_{n\to\infty} P(|\overline{X}-\mu|<\delta)\to 1. \quad (1)$$

Using the Lindeberg–Levy central limit theorem Eq. (1) becomes

$$P\left(-\frac{\delta\sqrt{n}}{\sigma}\le\frac{\overline{X}-\mu}{\sigma/\sqrt{n}}\le\frac{\delta\sqrt{n}}{\sigma}\right)=1-\varepsilon. \quad (2)$$

The right hand side is the $(1-\varepsilon)$ probability (confidence level) that standardized sample mean is within the specified interval. From (2), the number of observations is (Fig. 14d)

$$n=\left(z_{\varepsilon/2}\sigma\delta^{-1}\right)^2, \quad (3)$$

where z is inverse of the standard normal cumulative density function.

From the previous sections, the uncertainty of the LC mean separation period due to data processing biases is O(1mo). Fig. 14d shows that the number of observations that is necessary to approach the 1-month uncertainty level (related to biases in data processing) at 95% confidence level is ~100 separation events, which is roughly three times the number observed to date by altimetry, and nearly one and a half times the number simulated in the 54-year model experiment.

5. Discussion and summary

The LC state has been traditionally described in terms of several metrics derived from in situ and satellite observations of the upper ocean fields. Since the early 1990s, satellite altimetry data has been the primary source of information about mesoscale circulation in the GoM. The LC tracking algorithm of Leben (2005) is used to obtain different metrics of the LC and LCEs and to derive statistical estimates of these characteristics. Expected errors and uncertainties related to data collecting, data processing, and intrinsic variability of the LC system impact the statistical estimates of the LC state derived from altimeter observations. The major goal of this study is to assess the uncertainty of basic LC statistics derived from satellite observations. A free-running multidecadal numerical simulation of the GoM is employed to characterize sensitivity of the LC statistical estimates to various factors.

The LC variability in GoM-HYCOM simulation has been compared to the LC behavior from the altimeter-based data in terms of statistics of the LC northern and western extents, and statistics of the LCE separation period. The linear relation between the LCE separation period and the retreat latitude of the LC has also been tested. Evaluation of the major GoM characteristics (Yucatan flow and LC characteristics) in GoM-HYCOM has demonstrated a good agreement with the previous studies and altimeter observations. Despite some discrepancies between the observed and the model-estimated variability of the LC, statistical characteristics of the simulated LC are realistic.

GoM-HYCOM simulates interannual LC variability despite having climatological open boundaries. This result is consistent with the fundamental modeling study of LC variability by Hurlburt and Thompson (1980). In their numerical experiments, Hurlburt and Thompson (1980) demonstrate that quasi-annual, but not regular, eddy shedding occurred with a constant inflow rate prescribed at the open boundary. Pichevin and Nof (1997) explain the formation of LC eddies by a "momentum imbalance paradox". With an idealized model, they show that the eddy generation period decreases with increasing mass flux at the open boundary suggesting that irregular LC eddy shedding may be associated with varying transport in the Yucatan Channel. However, their model experiments are idealized. In reality, LC eddy shedding is more complex and less deterministic (Lugo-Fernandez, 2007). For example, mesoscale cyclones in the vicinity of the LC can impact the eddy shedding process (e.g., Cherubin et al., 2006). The existence of a large cyclonic eddy north of the LC can substantially delay the northward penetration of the LC, increasing the shedding time interval (Zavala-Hidalgo et al., 2006). These mesoscale processes are likely responsible for the variability of eddy shedding in the GoM-HYCOM.

Since the model mesoscale processes are well simulated, the model can be used to examine uncertainties of LC statistics estimated from the gridded satellite product that arise from limitations in the satellite sampling patterns and in the gridding and LC identification methodologies. The choice of the open boundary conditions with no interannual variability *a priori* limits the realism of the simulation, but this does not impact the major findings of this study. However, the open boundary conditions may have an impact on some aspects of the model variability, for example, the probability of retracted LC or the retreat latitude versus shedding period. Further insight is needed on the role of interannual variability of the Yucatan Channel flow in the LC interannual variability.

Uncertainty of altimeter-based LC statistics is assessed from a suite of sensitivity tests. Two tests have been performed to analyze the sensitivity of the LC statistics to the choice of reference mean SSH field and LC front definition. These sensitivity tests show that the LC statistics from the altimeter SSH fields is weakly sensitive to the choice of the reference SSH mean field (Fig. 9). Weak sensitivity of the LC statistics is also demonstrated in the test with alternative LC front definition (Fig. 8). In both cases, there are small changes in the distributions of the LC northern ($\le 0.1^\circ$) and western ($\le 0.2^\circ$) extent and LC separation period (≤ 0.5 month) compared to GoM-HYCOM. The number of LCE separation events is somewhat sensitive to the choice of the reference SSH field and front definition ranging from 65 to 68 events. The linear relationship between the separation period and the retreat latitude of the LC exhibits stronger sensitivity to these two tested uncertainties. Nevertheless, the regression slopes in these tests are statistically similar to those originally derived from GoM-HYCOM.

The LC statistics is more sensitive to satellite sampling patterns. The distributions of the northern and western LC extent from the satellite experiments (Figs. 10 and 11) look qualitatively disparate from GoM-HYCOM. Nevertheless, estimates of the mean LC northern and western extents across the satellite experiments slightly deviate ($\le 0.2^\circ$) from the original GoM-HYCOM estimates. Satellite sampling patterns has a more noticeable influence on the distribution and statistics of the LC eddy separation period (Fig. 12). The mean LCE separation period varies from 9.3 to 10.2 months across the experiments. The number of the LCE separation events varies from 63 to 69 in the satellite tests. The linear relation between the LCE separation period and the retreat latitude of the LC reveals high sensitivity to the LC statistics from the satellite experiments (Fig. 13), especially for single satellite sampling. SSH fields reconstructed from SSH anomalies sampled along synthetic satellite ground tracks are distorted and miss details of mesoscale features in the GoM present in the full SSH fields (Fig. 7b; in the animation: many cases, for example 3/24, 4/4, 4/9, etc.) Biases in the altimeter-based SSH fields stem from the spatial and temporal inhomogeneity of satellite observations especially with single satellite sampling. Short-lived small scale features are often missed in the interpolated SSH fields. For example, in Fig. 7b the LC front from the Topex experiment ("Topex" in Fig. 7) crosses a small cyclone on the eastern side of the LC neck. Obviously, the cyclone has been missed by the coarse spatial sampling from the 10-day repeat Topex orbit.

To summarize, analysis of the uncertainties in the LC statistics demonstrates that satellite sampling limits the accuracy of maps of LC mesoscale variability and is the largest contributor to uncertainties in the altimeter-based synthetic SSH fields. Increasing the number of satellites expectedly improves representation of the SSH fields and indicates a better agreement of the LC statistics with statistics from the original GoM-HYCOM simulation.

For practical application of the LC statistical estimates, it is important to assess reliability of these estimates. Whereas statistics of the LC extent seem to be robust, the LC separation mean

period exhibits remarkable variability in the observations. Different studies report different mean estimates of the LC separation period. The question is whether these changes in the estimates are random merely due to a stochastic behavior of the LC system or whether they manifest substantial changes in the LC system and its non-stationarity. In the latter case, the mean and variance of the LC are not well defined and the moments of the process cannot be estimated from the time series (von Storch and Zwiers, 1999). An answer to this question has important practical application because it defines whether observations of the LC system contain sufficient information to provide reliable parameter estimates (mean and variance or standard deviation of the LC separation period). The statistical tests (Section 4) cannot prove that the LC is non-stationary based on the LC statistics from the CCAR SSH fields over 1993–2010. Under the assumption of stationarity, the mean separation period estimated from CCAR data (1993–2010) is within (6.1–9.8) months at 95% confidence level. Stationarity and ergodicity of the process (Brockewell and Davis, 1991) need further investigation and longer observational records.

To analyze how statistical estimates vary in the model during the 54 years of integration and to see if model statistics exhibit a better agreement with the altimetry data during individual time intervals, LCE separation statistics are computed for overlapping 18-year segments (the number of years in the analyzed CCAR data) of the 54-year GoM-HYCOM-derived LC time series. The 18-year window is slid along the model data, providing 37 individual time series of separation periods. Statistics similar to the analysis in Section 4 are estimated for each 18-year segment (Fig. 15). The number of the eddy separation events per 18-year record ranges from 18 to 24 and remains below the estimate from CCAR altimetry (27). The 18-year mean separation period varies markedly among different segments mostly staying within the 95% confidence interval range of the mean separation period estimated from CCAR (Fig. 15a). Compared to CCAR (8 months), the separation periods from the model are predominantly longer. It is noteworthy that while 18-year mean separation periods vary over a wide range, the probability density functions of the separation periods are similar for each of the 18-year segments (not presented). The Kolmogorov–Smirnov test could not provide enough evidence to reject the hypothesis that any of the 37 distributions are the same. A one-way ANOVA F-test performed on three non-overlapping 18-year segments of the model data ($F_{2,62}=0.82$, p-value$=0.82$) cannot reject the null hypothesis that the means are the same. A similar result follows from the Levene's homoscedasticity test for the variance of the LC separation period ($F_{2,62}=1.05$, p-value$=0.35$). Thus, despite apparent variability of the LC statistics, the model cannot provide evidence of non-stationarity of the LC eddy separation process. Although, use of climatological open boundary conditions likely subdues interannual variability of the LC.

The linear relationship between the separation period and the retreat latitude of the LC is sensitive to the choice of an analyzed time segment (Fig. 15c). In some cases, the relationship in GoM-HYCOM is nearly as strong as in CCAR altimetry data (e.g., segments with model years 4–21, 5–22, 6–23, 7–24, 8–25, and 33–50). In other cases, the relationship is weakly linear (segments 17–34 through 31–48). For three segments (17–34, 18–35, and 20–37), the regression slopes are not significantly different from 0. It is noteworthy that both CCAR data (Fig. 14a and b) and (to a lesser extent) GoM-HYCOM indicate two distinct regimes in the LC separation period time series: longer periods with high variance and shorter separation periods with relatively narrow range of separation intervals. Due to the limited record length, one cannot conclude with confidence that these regimes are statistically different.

As a final point, this analysis has revealed some aspects of the model LC behavior that deviate from observations, and which may well have gone unnoticed from a cursory model-to-data comparison (e.g., simple comparison of means). The probability distribution of the

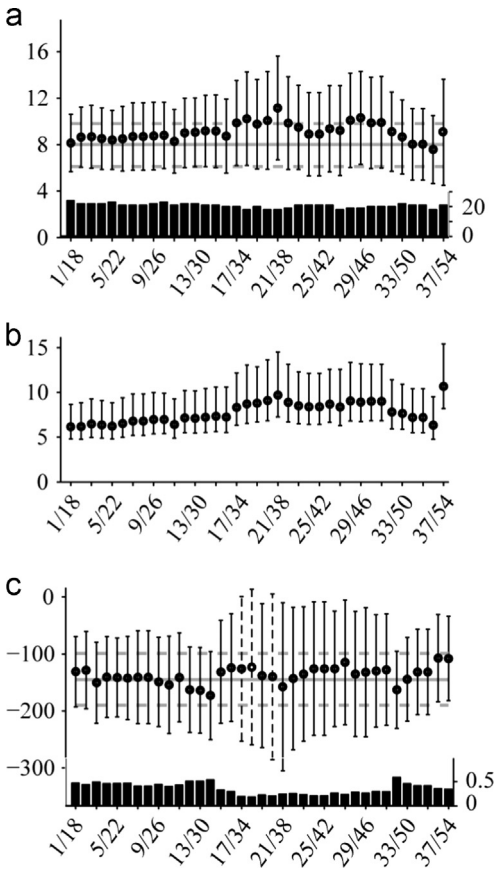

Fig. 15. LC statistics for overlapping 18-year segments of the 54-year GoM-HYCOM simulation. The numbers on the horizontal axis are model years of every 4th time segment: (a) mean separation period estimates (months) are shown with the black circles for each segment. The vertical lines are the 95% confidence intervals for the mean separation period. Horizontal gray solid and dashed lines are the mean separation period and the 95% confidence interval, respectively, for the CCAR data record (1993–2010). At the bottom, the bar diagram shows the number of separation events during the 18-year segments. (b) Standard deviation estimates and their 95% confidence intervals. (c) The slopes and 95% confidence intervals for the regression models of separation period versus the retreat latitude of the LC. Dashed significance bars designate statistically non-significant slopes. Horizontal gray solid and dashed lines are the slope and 95% confidence interval for the entire period of the analyzed CCAR data. At the bottom, the bar diagram presents the coefficients of determination for the regression model of separation period versus the retreat latitude of the LC following the previous eddy separation.

LC northern extent from the model is strongly bimodal (Fig. 5a). Although bimodality is evident in the altimetry (Fig. 4a) as well, the probability of the retracted mode is substantially weaker – an obvious discrepancy between the model and observations. It is noteworthy that distributions of the LC northern extent in all sensitivity experiments remain strongly bimodal (Figs. 8–10). This suggests that variability of the model LC has some inconsistency compared to the LC variability estimated from altimeter-based SSH. Also, the 4-year separation interval in GoM-HYCOM is intriguing and does not conform to the linear relationship between separation period versus the retreat latitude of the LC. A comprehensive analysis is necessary to understand these characteristics of the GoM-HYCOM simulation, which may provide new knowledge of LC dynamics while improving numerical simulations and applications of satellite altimeter observations of the GoM.

Acknowledgments

We would like to thank Dr. C. Cooper (Chevron Energy Technology Corp.) for his advice and motivation to develop the

54-year HYCOM simulation. We acknowledge O.M. Smedstad (QinetiQ North America – TSG Planning Systems, Inc.), E.J. Metzger, P.J. Hogan, and A.J. Wallcraft (NRL SSC) for providing forcing fields for the model experiment. This research was made possible by a grant from BP/The Gulf of Mexico Research Initiative to the Deep-C Consortium (SA 12-12, GoMRI-008), by the HYCOM consortium (N00014-09-1-0587), and a contract from Bureau of Ocean Energy Management (BOEM) (M12PC00003) to the FSU. This work was supported by a grant of computer time from the DoD High Performance Computing Modernization Program at NRL SSC. R. Leben and C. Hall acknowledge support from BOEM contracts M08PC20043 and M10PC00112 to Leidos Corporation. R. Leben also acknowledges support from NASA Ocean Surface Topography Mission Science Team Grants NNX08AR60G and NNX13AH05G.

Appendix A. Mean SSH terminology

In this study, "mean SSH" is referred to either as the temporal mean field averaged over a time interval T

$$\langle \eta \rangle = \frac{1}{T}\int_T \eta(x,y,t)dt \tag{A.1}$$

or the spatial mean field that is spatially averaged over an area A

$$\overline{\eta}(t) = \frac{1}{A}\iint_A \eta(x,y,t)dx\,dy \tag{A.2}$$

where $\eta(x,y,t)$ is SSH.

SSH fields defined as $\eta(x,y,t)-\langle\eta\rangle$ are referred to as "SSH anomaly" (SSHA). In this case, (A.1) can be thought of as a reference mean SSH.

Fields defined as $\eta(x,y,t)-\overline{\eta}$ are referred to as "demeaned SSH". Subtracting the spatial mean from the SSH is necessary to remove biases in the surface elevation fields for intercomparison. The spatially averaged SSH is calculated over the GoM deepwater where depths exceed 200 m in order to avoid contamination of the areal mean by high-frequency large-scale wind-forced coastal sea level anomalies (e.g., hurricane forced coastal-trapped waves). Sections B and C in Fig. 1a indicate approximate locations of the boundaries of the interior Gulf of Mexico within which (A.2) is calculated.

Appendix B. Kalman Filter algorithm for identification of the Loop Current front

In the following analysis, the assumption is made that the LC front closely follows the core of the LC. Under a geostrophic assumption, the core coincides with the maximum SSH gradient. Thus, the true LC front is determined by the maximum SSH gradient. Rationale of the suggested alternative approach for LC tracking is based on the idea of combining the knowledge about frontal position from two dynamic fields by employing the Kalman Filter technique (Kalman, 1960; Maybeck, 1979). In the described application, GoM-HYCOM SSH field provides the first guess of the LC front location (*a priori* estimate). GoM-HYCOM SSH gradient field ("measurement") is used to obtain the final frontal location (*a posteriori* estimate). Any other oceanographic field capable of capturing mesoscale structures can be used as a measurement.

In following the LC front from the Yucatan Channel to the Straits of Florida, the task is to estimate the next position along the contour $\mathbf{x}_k = [\varphi_k, \lambda_k]^T$ (φ and λ are coordinates) given the previous position $\mathbf{x}_{k-1}$. It is assumed that the process can be described by the linear stochastic difference equation

$$\mathbf{x}_k = \mathbf{A}\mathbf{x}_{k-1} + \mathbf{w}_{k-1}, \tag{B.1}$$

where $\mathbf{x}_k$ is the kth discrete position along the LC contour moving from Yucatan Channel to Florida Straits, $\mathbf{x}_{k-1}$ is the previous position, and $\mathbf{w}_{k-1}$ is the process noise. The matrix $\mathbf{A}$ relates the state at the previous step $(k-1)$ to the state at the current step k. The matrix $\mathbf{A}$ changes with each step. The prediction is corrected on the basis of a measurement, whose state is

$$\mathbf{z}_k = \mathbf{H}\mathbf{x}_k + \boldsymbol{\nu}_k. \tag{B.2}$$

The matrix $\mathbf{H}$ relates the current state to the measurement $\mathbf{z}_k$. In this application, $\mathbf{H}$ does not change. $\boldsymbol{\nu}_k$ represents the measurement noise.

Both random variables are assumed to be independent and normally distributed, $\mathbf{w} \sim N(0,\mathbf{Q})$ and $\boldsymbol{\nu} \sim N(0,\mathbf{R})$, where $\mathbf{Q}$ and $\mathbf{R}$ are process noise and measurement noise covariance matrices, respectively. They change at every step. Smaller $\mathbf{Q}$ or $\mathbf{R}$ suggests more confidence in predictions or measurements.

At every step, the *a priori* state estimate ($\hat{\mathbf{x}}_{k-1}^-$)at step k is obtained on the basis of knowledge of the process prior to step k. Then the *a priori* state is corrected on the basis of measurements, resulting in the *a posteriori* state estimate ($\hat{\mathbf{x}}_k^-$). Also defined are the *a priori* and *a posteriori* estimate errors

$$\mathbf{e}_k^- \equiv \mathbf{x}_k - \hat{\mathbf{x}}_k^- \tag{B.3}$$

$$\mathbf{e}_k \equiv \mathbf{x}_k - \hat{\mathbf{x}}_k. \tag{B.4}$$

Then *a priori* and *a posteriori* error covariance matrices are

$$\mathbf{P}_k^- = E[\mathbf{e}_k^- \mathbf{e}_k^{-T}], \tag{B.5}$$

$$\mathbf{P}_k = E[\mathbf{e}_k \mathbf{e}_k^T]. \tag{B.6}$$

An *a posteriori* state estimate $\hat{\mathbf{x}}_k$ is defined as a linear combination of an *a priori* estimate $\hat{\mathbf{x}}_k^-$ and a weighted difference between a measurement $\mathbf{z}_k$ and predicted measurement $\mathbf{H}\hat{\mathbf{x}}_k^-$ (also known as innovation or residual)

$$\hat{\mathbf{x}}_k = \hat{\mathbf{x}}_k^- + \mathbf{K}(\mathbf{z}_k - \mathbf{H}\hat{\mathbf{x}}_k^-). \tag{B.7}$$

The matrix $\mathbf{K}$ is the gain (blending) factor that minimizes the *a posteriori* error covariance (B.6)

$$\mathbf{K}_k = \mathbf{P}_k^- \mathbf{H}^T \left(\mathbf{H}\mathbf{P}_k^- \mathbf{H}^T + \mathbf{R}\right)^{-1}. \tag{B.8}$$

At every step, the LC tracking algorithm assesses the reliability of the *a priori* estimate and measurement depending on predefined criteria and changes $\mathbf{Q}$ and $\mathbf{R}$ accordingly.

The algorithm for identification of the LC using the Kalman Filter technique is as follows:

1) *Obtain the a priori state estimate*: The *a priori* state estimate (red dot in Fig. B1) is obtained by following in the direction perpendicular to the local SSH gradient from $\hat{\mathbf{x}}_{k-1}$ (red arrow in Fig. B1). Now matrix $\mathbf{A}$, which is required for projecting the error covariance matrix to the next step and is unknown at kth location, is estimated as

$$\mathbf{A} = \hat{\mathbf{x}}_k^- \left(\hat{\mathbf{x}}_{k-1}\right)^{-1}. \tag{B.9}$$

2) *Update* $\mathbf{Q}$: The process noise covariance $\mathbf{Q}$ and the measurement error covariance $\mathbf{R}$ are updated following a set of criteria to judge the trustworthiness of $\hat{\mathbf{x}}_k^-$ and $\mathbf{z}_k$. The SSH at the *a priori* estimate of the frontal location ($\eta_k = \eta(\hat{\mathbf{x}}_k^-)$) and SSH averaged over the previous five locations ($\overline{\eta}$) are used to update the process noise covariance $\mathbf{Q}$

$$C = \begin{cases} (1000|\eta_k - \overline{\eta}|)^{1.2} & \text{if } \eta_k \le \overline{\eta} \\ (1000|\eta_k - \overline{\eta}|)^{2} & \text{if } \eta_k > \overline{\eta} \end{cases} \tag{B.10}$$

$$\mathbf{Q} = C \cdot \mathbf{Q}_0,$$

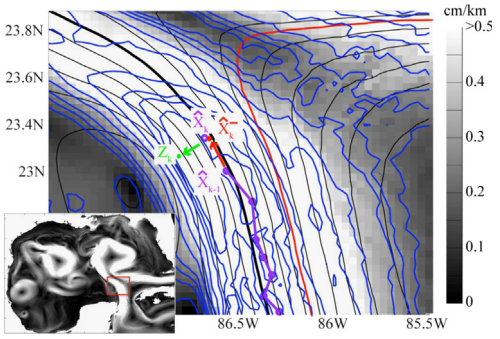

Fig. B1. LC identification algorithm based on the Kalman Filtering. The inset is GoM-HYCOM SSH gradient (cm/km) field in the Gulf of Mexico. The red box is the region where the LC tracking technique is illustrated. In the zoomed region, the background field (gray shading) is the SSH gradient (cm/km). The black and red lines are the 0.05-m and 0.17-m SSH contours, respectively. The blue lines are contours of the SSH gradient drawn at 0.1 cm/km intervals. The red dot is the *a priori* state estimates, the green dot is measurement, and the purple circles are the *a posteriori* state estimates of frontal locations at discrete positions. See text for more detail.

where

$$\mathbf{Q}_0 = \begin{pmatrix} 0.01 & 0 \\ 0 & 0.01 \end{pmatrix}$$

agrees with the uncorrelated process noise assumption.

3) *Project the error covariance from state $k-1$ to k*

$$\mathbf{P}_k^- = \mathbf{A}\mathbf{P}_{k-1}\mathbf{A}^T + \mathbf{Q} \tag{B.11}$$

4) *Obtain measurement location*: The measurement of the frontal location $\mathbf{z}_k$ (green dot Fig. B1) is given by the local maximum of the SSH gradient ($|\nabla\eta|_{max}$). The local maximum is searched in the direction (green arrow in Fig. B1) determined by the local second derivative of the SSH at the *a priori* location ($\hat{\mathbf{x}}_k^-$).

5) *Update* **R**: Local SSH is obtained for measurement location $\mathbf{z}_k$ ($\eta_z = \eta(\mathbf{z}_k)$) and **R** is updated as

$$c_0 = 100|\eta_k - \eta_z| \tag{B.12}$$

$$C = c_0 \exp\lfloor (D_{AO} \times 10^{-4})^{1.2} \rfloor \tag{B.13}$$

$$\mathbf{R} = C\,\mathbf{R}_0, \tag{B.14}$$

where D_{AO} is distance (m) between $\hat{\mathbf{x}}_k^-$ and $\mathbf{z}_k$, and

$$\mathbf{R}_0 = \begin{pmatrix} 0.01 & 0 \\ 0 & 0.01 \end{pmatrix}.$$

6) *Compute the Kalman gain*: Eq. (B.8) is used. The matrix **H** is

$$\mathbf{H} = \begin{pmatrix} 1 & 0 \\ 0 & 1 \end{pmatrix}. \tag{B.15}$$

This design of **H** means that in the absence of process error and measurement error, the process is identical to the measurement.

7) *Update the a priori estimate* using (B.7) *to obtain the a posteriori estimate.*

8) *Update the error covariance*

$$\mathbf{P}_k = \mathbf{P}_k^- - \mathbf{K}_k\mathbf{H}\mathbf{P}_k^-. \tag{B.16}$$

Steps 1–9 are then repeated to obtain the next discrete location along the LC front.

Appendix C. CCAR altimeter data processing

CCAR GoM SSH dataset used in this study is a subset the 20-year record derived from reprocessing of archival altimeter data streams for the BOEM Environmental Studies Program: "Observations and Dynamics of the Loop Current in U.S. Waters". The altimeter data processing is based on near real-time mesoscale analysis techniques that are designed to exploit multi-satellite altimetric sampling (Leben et al., 2002). This processing system has been used to operationally monitor the GoM since November 1995. The system was updated to allow processing of along track altimeter data collected from the Radar Altimeter Database System (RADS) hosted by the Delft Institute of Earth Observation and Space Systems at the Delft University of Technology in the Netherlands. RADS (Naeije et al., 2008, 2000) is an online database that contains validated and verified altimeter data and correction data products for historical and operational satellite altimeter missions. A detailed description of the processing of the GoM SSH dataset can be found in Hamilton et al. (2015). The same software system was used to process the simulated along track altimeter data from GoM-HYCOM with the modifications to the processing described in Section 2.3 of this paper.

Appendix D. Supporting information

Supplementary data associated with this article can be found in the online version at: http://dx.doi.org/10.1016/j.dsr.2015.01.005.

References

Abascal, A.J., Sheinbaum, J., Candela, J., Ochoa, J., Badan, A., 2003. Analysis of flow variability in the Yucatan Channel. J. Geophys. Res. 108 (C12), 3381. http://dx.doi.org/10.1029/2003JC001922.

Andrade-Canto, F, Sheinbaum, J.., Sanson, L.Z., 2013. A Lagrangian approach to the Loop Current eddy separation. Nonlinear Process. Geophys. 20 (1), 85–96.

Bleck, R., 2002. An oceanic general circulation model framed in hybrid isopycnic-Cartesian coordinates. Ocean Model. 4, 55–88.

Brockewell, P.J., Davis, R.A., 1991. Time Series: Theory and Methods, 2nd edition Springer-Verlag p. 571.

Bunge, L., Ochoa, J., Badan, A., Candela, J., Sheinbaum, J., 2002. Deep flows in the Yucatan Channel and their relation to changes in the Loop Current extension. J. Geophys. Res. 107 (C12), *3233*. http://dx.doi.org/10.1029/2001JC001256.

Chang, Y.-L., Oey, L.-Y., 2013. Loop Current growth and eddy shedding using models and observations: numerical process experiments and satellite altimetry data. J. Phys. Oceanogr. 43, 669–689. http://dx.doi.org/10.1175/JPO-D-12-0139.1.

Chassignet, E.P., Smith, L.T., Halliwell, G.R., Bleck, R., 2003. North Atlantic simulation with the HYbrid Coordinate Ocean Model (HYCOM): impact of the vertical coordinate choice, reference density, and thermobaricity. J. Phys. Oceanogr. 33, 2504–2526.

Chassignet, E.P., Hurlburt, H.E., Smedstad, O.M., Halliwell, G.R., Wallcraft, A.J., Metzger, E.J., Blanton, B.O., Lozano, C., Rao, D.B., Hogan, P.J., Srinivasan, A., 2006. Generalized vertical coordinates for eddy-resolving global and coastal ocean forecasts. Oceanography 19 (1), 20–31.

Chelton, D.B., Ries, J.C., Haines, B.J., Fu, L.L., Callahan, P.S., 2001. Satellite altimetry. In: Fu, L.L., Cazename, A. (Eds.), Satellite Altimetry and Earth Sciences. Academic Press, San Diego, CA, USA, pp. 1–122.

Chelton, D., Schlax, M.G., Samelson, R.M., 2011. Global observations of nonlinear mesoscale eddies. Prog. Oceanogr. 91, 167–216.

Cherubin, L.M., Morel, Y., CHassignet, E.P., 2006. Loop Current ring shedding: the formation of cyclones and the effect of topography. J. Phys. Oceanogr. 36 (4), 569–591.

de Leeuw, W.C., Post, F.H., 1995. A statistical view on vector fields. In: Göbel, M., Müller, H., Urban, B. (Eds.), Visualization in Scientific Computing, Eurographics. Springer-Verlag, Wien, pp. 53–62.

Dibarboure, G., Pujol, M.-I., Briol, F., Le Traon, P.Y., Larnicol, G., Picot, N., Mertz, F., Ablain, M., 2011. Jason-2 in DUACS: updated system description, first tandem results and impact on processing and products. Mar. Geodesy 34 (3–4), 214–241.

DiMarco, S.F., Nowlin Jr., W.D., Reid, R.O., 2005. A statistical description of the velocity fields from upper ocean drifters in the Gulf of Mexico. In: Sturges, W., Lugo-Fernandez, A. (Eds.), circulation in the Gulf of Mexico: observations and Models. AGU, Washington, DC, pp. 101–110. http://dx.doi.org/10.1029/161GM08.

Donohue, K., Hamilton, P., Leben, R., Watts, R., Waddell, E., 2008. Survey of Deepwater Currents in the Northwestern Gulf of Mexico, vol. II: Technical Report. OCS Study MMS 2008-031. U.S. Department of the Interior, Minerals Management Service, Gulf of Mexico OCS Region, New Orleans, 364 pp.

Ezer, T., Oey, L.-Y., Lee, H.-C., Sturges, W., 2003. The variability of currents in the Yucatan Channel: analysis of results from a numerical ocean model. J. Geophys. Res. 108 (C1), 3012. http://dx.doi.org/10.1029/2002JC001509.

Forristall, G.Z., Leben, R.R., Hall, C.A., 2010. A statistical hindcast and forecast model for the loop current. In: Proceedings of the Offshore Technology Conference, 3–6 May 2010, Houston, TX, USA. Paper OTC-20602-MS, 12 pp., http://dx.doi.org/10.4043/20602-MS.

Hamilton, P., Donohue, K., Hall, C., Leben, R. R., Quian, H., Sheinbaum, J., Watt, D. R., 2015. Observations and Dynamics of the Loop Current. Technical Report. OCS Study BOEM 2015-006. U.S. Department of the Interior, Bureau of Ocean Energy Management, Gulf of Mexico OCS Region, New Orleans, LA, 257 pp.

Hartigan, J.A., Hartigan, P.M., 1985. The dip test of unimodality. Ann. Stat. 13 (1), 70–84.

Hurlburt, H.E., Thompson, J.D., 1980. A numerical study of Loop Current intrusions and eddy shedding. J. Phys. Oceanogr. 10, 1611–1651.

Jennrich, R.I., 1995. An Introduction to Computational Statistics: Regressions Analysis. Prentice-Hall, New Jersey p. 364.

Kalman, R.E., 1960. A new approach to linear filtering and prediction problems. Trans. ASME–J. Basic Eng. 82 (Series D), 35–45.

Kantha, L., Choi, J.-K., Schaudt, K.J., Cooper, C.K., 2005. A regional data-assimilative model for operational use in the Gulf of Mexico. In: Sturges, W., Lugo-Fernandez, A. (Eds.), Circulation in the Gulf of Mexico: Observations and Models. Geophysical Monograph, 161. American Geophysical Union, Washington, DC, pp. 165–180.

Kara, A.B., Rochford, P.A., Hurlburt, H.E., 2000. Efficient and accurate bulk parameterizations of air–sea fluxes foruse in general circulation models. J. Atmos. Ocean. Technol. 17, 1421–1438.

Lanzante, A, 2005. Cautionary note on the use of error bars. J. Clim. 18, 3699–3703.

Leben, R.R., Born, G.H., Engebreth, B.R., 2002. Operational altimeter data processing for mesoscale monitoring. Mar. Geodesy 25, 3–18.

Leben, R.R., 2005. Altimeter-derived Loop Current metrics. In: Sturges, W., Lugo-Fernandez, A. (Eds.), Circulation in the Gulf of Mexico: Observations and Models. AGU, Washington, DChttp://dx.doi.org/10.1029/161GM15.

Levene, H., 1960. Robust tests for equality of variances. In: Olkin, I., Hoteling, H., et al. (Eds.), Contributions to Probability and Statistics: Essays in Honor of Harold Hotelling. Stanford University Press, Palo Alto, CA, pp. 278–292.

Lugo-Fernandez, A., 2007. Is the Loop Current a chaotic oscillator? J. Phys. Oceanogr. 37, 1455–1469.

Lugo-Fernandez, Leben, 2010. On the linear relationship between Loop Current Retreat Latitude and Eddy Separation period. J. Phys. Oceanogr. 40 (12), 2778–2784.

Lindo-Atichati, D., Bringas, F., Goni, G., 2013. Loop Current excursions and ring detachments during 1993–2009. Int. J. Remote Sens. 34 (14), 5042–5053.

Massey, F.J., 1951. The Kolmogorov–Smirnov Test for Goodness of Fit. J. Am. Stat. Assoc. 46 (253), 68–78.

Maul, G.A., 1977. The annual cycle of the Gulf Loop Current. Part 1: observations during a one-year time series. J. Mar. Res. 35, 29–47.

Maybeck, P.S., 1979. Stochastic Models, Estimation, and Control, vol. 1. Academic Press, Inc, New York.

Naeije, M., Schrama, E., Scharroo, R., 2000. The radar altimeter database system project RADS. Proceedings of the International Geoscience and Remote Sensing Symposium (IGARSS) 2000, vol. 2 , http://dx.doi.org/10.1109/IGARSS.2000.861605.

Naeije, M., Scharroo, R., Doornbos, E., Schrama, E., 2008. Global Altimetry Sea-level Service: GLASS. Final Report. NIVR/DEOS publ., NUSP-2 report GO 52320 DEO, 107 pp.

Nason, G.P., 2006. Stationary and non-stationary time series. In: Mader, H.M., Coles, S.G., Connor, C.B., Connor, L.J. (Eds.), Statistics in Volcanology. Geological Society for IAVCEI, UK, pp. 129–142.

Nedbor-Gross, R., Dukhovskoy, D.S., Bourassa, M.A., Morey, S.L., Chassignet, E., 2014. Investigation of the relationship between the Yucatan Channel transport and the Loop Current area in a multi-decadal numerical simulation. MTS J. 48 (4), 15–26.

Nowlin Jr., W.D., Jochens, A.E., DiMarco, S.F., Reid, R.O, Howard, M.K., 2001. Deepwater Physical Oceanography Reanalysis and Synthesis of Historical Data: Synthesis Report. U.S. Department of the Interior, Minerals Management Service, Gulf of Mexico OCS Region, New Orleans, LA. OCS Study MMS 2001-064. 530 pp.

Payton, M.E., Greenstone, M.H., Shenker, N., 2003. Overlapping confidence intervals or standard error intervals: what do they mean in terms of statistical significance? J. Insect Sci. 3 (34), 1–6.

Pichevin, T., Nof, D., 1997. The momentum imbalance paradox. Tellus 49A, 298–319.

Rice, J.A., 1995. Mathematical Statistics and Data Analysis. Duxbury Press, Wadsworth Publishing Company, Belmont, CA, USA, pp. 53–62.

Rosmond, T.E., Teixeira, J., Peng, M., Hogan, T.F., Pauley, R., 2002. Navy operational global atmospheric predictions system (NOGAPS): forcing for ocean models. Oceanography 15 (1), 99–108.

Rousset, C., Beal, L.M., 2010. Observations of the Florida and Yucatan Currents from a Caribbean cruise ship. J. Phys. Oceanogr. 40, 1575–1581. http://dx.doi.org/10.1175/2010JPO4447.1.

Sadarjoen, I.A., Post, F.H., 2000. Detection, quantification, and tracking of vortices using streamline geometry. Comput. Graph. 24, 333–341.

Saha, S., Moorthi, S.S., Pan, H.-L., Wu, X., Wang, J., Nadiga, S., Tripp, P., Kistler, R., Woollen, J., Behringer, D., Liu, H., Stokes, D., Grumbine, R., Gayno, G., Wang, J., Hou, Y.-T., Chuang, H.-Y., Juang, H.-M., Sela, J., Iredell, M., Treadon, R., Kleist, D., van Delst, P., Keyser, D., Derber, J., Ek, M., Meng, J., Wei, H., Yang, R., Lord, S., van den Dool, H., Kumar, A., Wang, W., Long, C., Chelliah, M., Xue, Y., Huang, B., Schemm, J.-K., Ebisuzaki, W., Lin, R., Xie, P.P., Chen, M., Zhou, S., Higgins, W., Zou, C.-Z., Liu, Q., Chen, Y., Han, Y., Cucurull, L., Reynolds, R.W., Rutledge, G., Goldberg, M., 2010. The NCEP climate forecast system reanalysis. Bull. Am. Meteor. Soc. 91, 1015–1057. http://dx.doi.org/10.1175/2010Bams3001.1.

Schilling, M.F., Watkins, A.E., Watkins, W., 2002. Is human height bimodal? Am. Stat. 56 (3), 223–229.

Sheinbaum, J., Candela, J., Badan, A., Ochoa, J., 2002. Flow structure and transports in the Yucatan Channel. Geophys. Res. Lett. 29 (3), 1040. http://dx.doi.org/10.1029/2001GL0139990.

Shum, C.K., Ries, J.C., Tapley, B.D., 1995. The accuracy and applications of satellite altimetry. Geophys. J. Int. 121, 321–336.

Sturges, W., 1994. The frequency of ring separation from the Loop Current in the Gulf of Mexico. J. Mar. Res. 41, 639–653.

Sturges, W., Evans, J.C., 1983. On the variability of the Loop Current in the Gulf of Mexico. J. Mar. Res. 41 (4), 639–653.

Sturges, W., Leben, R.R., 2000. Frequency of ring separation from the Loop Current in the Gulf of Mexico. J. Phys. Oceanogr. 30, 1814–1819.

von Storch, H., Zwiers, F.W., 1999. Statistical Analysis in Climate Research. Cambridge University Press p. 484.

Vukovich, F.M., 1995. An updated evaluation of the Loop Currents eddy shedding frequency. J. Geophys. Res. 100 (C5), 8655–8659.

Vukovich, F.M., 2007. Climatology of ocean features in the Gulf of Mexico using satellite remote sensing data. J. Phys. Oceanogr. 37, 689–707. http://dx.doi.org/10.1175/JPO2989.1.

Vukovich, F.M., 2012. Changes in the Loop Current's Eddy shedding in the period 2001–2010. Int. J. Oceanogr. 2012, 1–18.

Wunsch, C., Stammer, D., 1998. Satellite altimetry, the marine geoid, and the oceanic general circulation. Annu. Rev. Earth Planet. Sci. 26, 219–253.

Zamudio, L., Hogan, P.J., 2008. Nesting the Gulf of Mexico in Atlantic HYCOM: oceanographic processes generated by Hurricane Ivan. Ocean. Model. 21, 106–125.

Zavala-Hidalgo, J., Morey, S.L., O'Brien, J.J., Zamudio, L., 2006. On the Loop Current eddy shedding variability. Atmosfera 19 (1), 41–48.